UNIVERSIDADE FEDERAL DE SÃO CARLOS
PROGRAMA DE PÓS GRADUAÇÃO EM FÍSICA

Igor Ricardo Filgueira e Silva

Unveiling the Nature of Nonequilibrium Effects in Dielectrics

São Carlos - SP, Brazil

February 28, 2025

Igor Ricardo Filgueira e Silva

Unveiling the Nature of Nonequilibrium Effects in Dielectrics

Master's thesis submitted to the Graduate Program of Physics at the Universidade Federal de São Carlos, in partial fulfillment of the requirements for obtaining the degree of Master of Science in Physics.

Universidade Federal de São Carlos – UFSCar

Centro de Ciências Exatas e de Tecnologia – CCET

Programa de Pós-graduação em Física – PPGF

Supervisor: Prof. Dr. Victor Lopez-Richard

São Carlos - SP, Brazil

February 28, 2025

Igor Ricardo Filgueira e Silva

Unveiling the Nature of Nonequilibrium Effects in Dielectrics

Master's thesis submitted to the Graduate Program of Physics at the Universidade Federal de São Carlos, in partial fulfillment of the requirements for obtaining the degree of Master of Science in Physics.

Graduate Advisory Committee:

Prof. Dr. Victor Lopez-Richard
Supervisor

Prof. Dra. Lilian Menezes de Jesus
Committee Member 1

Prof. Dr. Roger Gomes Fernandes
Committee Member 2

Date defended/Approved: 28/02/2025

São Carlos - SP, Brazil
February 28, 2025

To Sandra, Josias, Patrícia, Davi and Paulinho, my family.

Acknowledgments

First, I would like to express my sincere gratitude to my advisor, Professor Victor Lopez-Richard, for his invaluable knowledge, unwavering support, and insightful guidance throughout this journey. His patience and dedication have been fundamental in shaping this work, and without his expertise and encouragement, this dissertation would not have reached the same level of depth and rigor. I am truly grateful for the opportunity to learn under his mentorship, which has profoundly contributed to my academic and professional growth.

I also want to express my heartfelt gratitude to my family, especially my father, Josias, and my mother, Sandra. Throughout these years, many challenges and milestones have come and gone, but you have always been by my side, sometimes holding my hand, always encouraging me to keep going and never give up. Even though I have been far from home, you have never been far from my thoughts. Your unwavering love and support have been my foundation, and for that, I am forever grateful. Paulinho, Davi, and Patrícia, thank you for all the hugs, support and for always being there.

My thanks also go to my friends: Teonas, a lifelong friend who has always supported my wild ideas; Matheus, the friend that physics gave me, ten years later, look at where we are; Milena, the friend that São Carlos brought into my life, sweeping through infinities with me; and Bruna, Giovanna, and Vinícius, eight years of virtual friendship, yet your presence has always been real. Thank you for being here for another milestone. Your friendship has been a source of strength and joy throughout this journey, and I am deeply thankful for each of you, as well as all the other friends who have been by my side along the way.

I am also grateful to my research group for all the Friday meetings where we discussed physics and many other things. Your insights, support, and camaraderie have been invaluable in shaping this work and making this journey even more meaningful.

Finally, my deepest thanks to the Programa de Pós-Graduação em Física (PPGF), Universidade Federal de São Carlos (UFSCar) for enabling me to pursue this master's degree with intellectual and structural support possible, and also to Coordenação de Aperfeiçoamento de Pessoal de Nível Superior (CAPES) for the financial support provided through a master's scholarship (process number: 88887.841274/2023-00).

"Nunca esqueça quem você é.
O resto do mundo não vai esquecer.
Use isso como armadura, e nunca poderá
ser usado para te machucar." – Tyrion Lanister

(As Crônicas de Gelo e Fogo: A Guerra dos Tronos - George R. R. Martin)

Resumo

Este trabalho apresenta um modelo teórico abrangente para descrever a dinâmica de geração e aprisionamento de cargas em não equilíbrio em materiais dielétricos sob efeitos de fuga, sem a necessidade de suposições prévias sobre o tipo específico do material. Como resultado, ele se aplica a sistemas não polares e não ferroelétricos que, no entanto, exibem histerese em sua resposta dielétrica. Esse comportamento emergente surge de distribuições de energia de barreira, efeitos de polaridade da tensão e assimetrias nas taxas de transferência de carga, fornecendo novas perspectivas sobre os mecanismos que podem imitar respostas semelhantes às ferroelétricas em dielétricos com fuga. Uma compreensão mais profunda dessas propriedades é crucial para o avanço de dispositivos semicondutores, contribuindo para sua eficiência, confiabilidade e miniaturização aprimoradas. Além disso, as semelhanças marcantes entre os efeitos descritos pelo modelo e aqueles observados em materiais ferroelétricos abrem novas perspectivas para aplicações inovadoras, incluindo memórias não voláteis, sensores avançados e novos componentes eletrônicos. Esta dissertação também apresenta uma solução analítica que corrobora os resultados experimentais, fornecendo uma análise espectral detalhada da impedância e da permissividade dielétrica por modos. Ao unificar essas duas abordagens em uma única estrutura teórica, este trabalho oferece uma metodologia mais rigorosa para caracterizar materiais dielétricos e suas propriedades de transporte. Além de sua relevância para a caracterização dielétrica, o modelo foi aplicado com sucesso à definição e realização de Mem-emissores – dispositivos optoeletrônicos que modulam a emissão de luz através de variáveis de estado internas. Ao demonstrar a ligação entre as flutuações de polarização dielétrica e a dinâmica de transição óptica, este trabalho estabelece uma base teórica para o desenvolvimento de sistemas emissores de luz programáveis com aplicações potenciais em computação neuromórfica e circuitos fotônicos adaptáveis. Os resultados obtidos sugerem que este modelo fornece uma descrição abrangente da dinâmica de carga e das respostas dielétricas macroscópicas, oferecendo uma nova perspectiva para investigar efeitos de não equilíbrio em dielétricos. Esta base teórica abre caminho para futuras pesquisas em ciência dos materiais, física de semicondutores e dispositivos eletrônicos e optoeletrônicos de próxima geração.

Palavras-chave: Materiais dielétricos, dinâmica de cargas de não-equilíbrio, capacitor, polarização, corrente, histereses, análise de impedância, permissividade dielétrica, relaxor ferroelétrico, memoristor e mem-emissor.

Abstract

This work presents a comprehensive theoretical model for describing the generation and trapping dynamics of nonequilibrium charges in dielectric materials under leakage effects, without requiring prior assumptions about the material's specific type. As a result, it applies to nonpolar and non-ferroelectric systems that nonetheless exhibit hysteresis in their dielectric response. This emergent behavior arises from barrier energy distributions, voltage polarity effects, and asymmetries in charge transfer rates, providing new insights into mechanisms that can mimic ferroelectric-like responses in leaky dielectrics. A deeper understanding of these properties is crucial for advancing semiconductor devices, contributing to their improved efficiency, reliability, and miniaturization. Furthermore, the striking similarities between the effects described by the model and those observed in ferroelectric materials open new perspectives for innovative applications, including nonvolatile memories, advanced sensors, and novel electronic components. This dissertation also presents an analytical solution that corroborates experimental findings, providing a detailed spectral analysis of impedance and dielectric permittivity by modes. By unifying these two approaches within a single theoretical framework, this work offers a more rigorous methodology for characterizing dielectric materials and their transport properties. Beyond its relevance to dielectric characterization, the model has been successfully applied to the definition and realization of Mem-emitters – optoelectronic devices that modulate light emission through internal state variables. By demonstrating the link between dielectric polarization fluctuations and optical transition dynamics, this work establishes a theoretical foundation for the development of programmable light-emitting systems with potential applications in neuromorphic computing and adaptive photonic circuits. The results obtained suggest that this model provides a comprehensive description of charge dynamics and macroscopic dielectric responses, offering a novel perspective for investigating nonequilibrium effects in dielectrics. This theoretical foundation paves the way for future research in material science, semiconductor physics, and next-generation electronic and optoelectronic devices.

Keywords: Dielectric materials, nonequilibrium charge dynamics, capacitor, polarization, current, hysteresis, impedance analysis, dielectric permittivity, relaxor ferroelectric, memristor, and mem-emitter.

List of Figures

List of Tables

List of symbols

p	Dipole moment
r_i	Charges position
dq_1	Infinitesimal charge
P	Polarization
Ω	Dieletric's volume
d	Size of the capacitor
A	Area of the capacitor plates
γ	Index indicating the type of dynamics
(p)	Index to internal polarization
(lk)	Index to leakage effect
$F_j^{(\gamma)}$	Charge flux across barriers
$E^{(\gamma)}$	Barrier energy of indicate index
η	Efficiency
L	Size of site
β	Saturation parameter
V	Voltage applied
v	Velocity of the particles
m^*	Effective Mass
k_B	Boltzmann Constant
T_{eff}	Effective temperature
$D(E)$	Density of states
$f_{FD}(E, \mu)$	Fermi-Dirac distribution
$\mu_j^{(\gamma)}$	Barrier potential

E	Electric field
n	Number of particles per unit volume
D	Electric displacement
ε_0	Electric permittivity in vacuum
χ_∞	Susceptibility
I	Current total
C	Capacitance
j_D	Current Displacement
$\hbar$	Reduced Planck constant
$\delta P^{(\gamma)}$	Fluctuation in polarization
$\partial P/\partial t\|^{(\gamma)}$	Polarization transfer function
$\tau^{(\gamma)}$	relaxation time
G_0	Unperturbed conductance
δn	Number of *non-equilibrium* carriers
Y	Admittance
Z	Impedance
G	Conductance
B	Susceptance
R	Resistance
T	Period

Contents

1 Introduction

Dielectric materials are characterized by their ability to store electrical energy in an electric field. This property arises from their insulating nature, which impedes the flow of free charges, and their inherent polarizability, the ability of their constituent atoms or molecules to become electrically polarized in the presence of an electric field [1–3]. Dielectrics are essential components in a wide range of electrical and electronic devices, including capacitors, insulators in transistors, and various components in high-frequency circuits [3–5]. While often used in conjunction with semiconductor materials, which enable controlled charge flow, dielectrics serve a fundamentally different purpose: they provide electrical insulation and enable energy storage, rather than charge conduction.

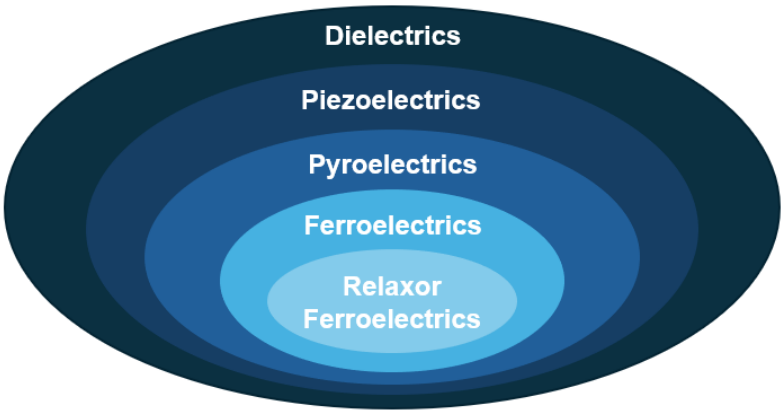

Figure 1 – Diagram depicting some subgroups of dielectric materials, including piezoelectric, pyroelectric, ferroelectric, and relaxor ferroelectric materials.

Dielectric materials comprise several categories, each characterized by distinct properties and functionalities [6]. As illustrated in Figure 1, piezoelectric, pyroelectric, and ferroelectric materials are notable examples, all demonstrating unique electromechanical and thermal responses.

Piezoelectric materials possess a crystal structure that lacks a center of symmetry, enabling a remarkable coupling between mechanical stress and electrical polarization. When subjected to mechanical stress, these materials generate an electrical charge, a phenomenon known as the direct piezoelectric effect [7]. Conversely, applying an electric field to a piezoelectric material induces mechanical deformation, known as the converse piezoelectric effect.

Pyroelectric materials represent a subset of piezoelectrics. In addition to the piezoelectric effect, pyroelectrics exhibit a change in spontaneous electrical polarization with temperature variations [8–10]. This temperature-dependent polarization change leads to the generation of an electrical charge when the material is heated or cooled. All

pyroelectric materials are also piezoelectric, as their crystal structure inherently allows for the stress-induced charge generation. Pyroelectric materials find applications in thermal sensing, infrared detectors, and energy harvesting.

Ferroelectric materials form a special class within pyroelectrics. They possess a spontaneous electric polarization that, unlike typical pyroelectrics, can be reversed by applying an external electric field [11]. This switchable polarization is the hallmark of ferroelectricity and leads to a characteristic hysteresis loop in the polarization-electric field response. Consequently, all ferroelectric materials are both pyroelectric and piezoelectric. The ability to switch polarization makes ferroelectrics attractive for applications such as non-volatile memory, ferroelectric capacitors, and electro-optic devices. [12–20]

Within ferroelectrics, there is a subcategory known as relaxor ferroelectrics, which is primarily characterized by three factors: their dielectric permittivity, which is temperature-dependent and exhibits a broad, diffuse maximum value. This maximum is also influenced by the sweep voltage frequency, with a notable dependency on it. Moreover, unlike other ferroelectric materials, relaxors do not undergo symmetry breaking with temperature changes [21]. Despite their differences, research on relaxors has been progressing, highlighting their essential role in advancing electronic devices [22–24].

While polarization-electric field hysteresis loops are a widely used tool for characterizing ferroelectricity, interpreting these curves requires caution. Apparent ferroelectric behavior can sometimes result from extrinsic mechanisms, such as interface effects or charge trapping, which can mimic true ferroelectricity [25–27]. Therefore, a rigorous analysis, complemented by additional characterization techniques, is essential to definitively confirm the ferroelectric nature of a material. Rather than solely focusing on intrinsic ferroelectric responses, an equally significant yet often overlooked topic is the investigation of potential sources of apparent ferroelectric behaviors. These include not only characteristic signatures in polarization-voltage and current-voltage loops but also relaxor-like responses as a function of temperature.

Thus, understanding the properties of dielectric and polar materials is essential for both theoretical and experimental advancements. The contributions presented in this work significantly enhance the study of dielectric properties and behaviors by providing new insights into dielectric responses, charge transport mechanisms, polarization dynamics, and spectral analysis. These insights stem from the investigation of nonequilibrium dynamics and leakage effects occurring within these materials.

Dielectric materials, despite their intrinsic insulating nature, exhibit complex behaviors when subjected to external perturbations, particularly in the presence of leakage currents and charge trapping mechanisms. Traditional models often assume equilibrium conditions, overlooking the transient and dynamic responses that arise in real systems. This work bridges this gap by combining electrochemical impedance spectroscopy, dielectric

spectroscopy, and voltammetry to explore microscopic mechanisms in poorly conductive systems dominated by displacement currents. These methodologies allow for the precise characterization of dipole relaxation and charge transport phenomena, revealing fundamental aspects of polarization dynamics in leaky dielectrics.

Furthermore, recent advances in nanoscale optoelectronics and quantum materials have introduced new paradigms for understanding memory effects in dielectric systems. Inspired by the physics of memristors [28–30] and resistive switching [31], this study extends the concept of nonequilibrium charge dynamics to optoelectronic devices. In particular, the emergence of mem-emitters—devices [32] that exploit hysteretic light-emission properties in transition-metal dichalcogenide-based heterostructures—provides a novel perspective on how charge dynamics influence macroscopic observables. These phenomena, which manifest as optical memory effects, further emphasize the need to develop comprehensive models that integrate both electrical and optical responses of dielectric materials under nonequilibrium conditions. The emergence of optical memory and the distinctive properties of memristors make them indispensable for neuromorphic computing [33] and a wide range of cutting-edge applications, including adaptive electronics, reconfigurable circuits, and quantum computing [34–36].

A key aspect explored in this work is the interplay between charge trapping, leakage currents, and polarization switching in non-ferroelectric materials, which can often mimic ferroelectric-like behavior. The analysis presented herein provides a theoretical framework that explicitly incorporates these effects, allowing for the accurate interpretation of complex dielectric responses. By integrating insights from both microscopic modeling and experimental techniques, this study offers a deeper understanding of the fundamental mechanisms governing nonequilibrium effects in dielectrics. This knowledge is crucial for optimizing the performance of dielectric-based devices, including capacitors, memory elements, and optoelectronic systems, paving the way for new technological advancements in energy storage, sensing, and communication applications.

This dissertation has contributed to three published scientific articles, each addressing key aspects of nonequilibrium effects in dielectric and optoelectronic systems:

- "Microscopic Modeling of Polarization Dynamics in Leaky Dielectrics: Insights into Ferroelectric-Like Behavior". Published in **Materials Science & Engineering B**, this work presents a theoretical framework for understanding polarization dynamics in leaky dielectrics, highlighting mechanisms that can mimic ferroelectric behavior [37].
- "The Emergence of Mem-Emitters". Published in **Nano Letters**, this study explores the concept of mem-emitters, devices that exhibit memory effects in light emission, bridging the fields of memristive and optoelectronic systems [32].
- "Optical Memory in a $MoSe_2$/Clinochlore Device". Published in **ACS Applied**

Materials & Interfaces, this article investigates optical memory phenomena in two-dimensional heterostructures, demonstrating how charge trapping and polarization effects contribute to persistent optical states [38].

1.1 Motivation and Objectives

The primary motivation of this master's dissertation is to introduce new perspectives within a robust theoretical framework, advancing the understanding of nonequilibrium effects in dielectric materials. These materials are fundamental to modern electronics, influencing everything from energy storage devices to emerging optoelectronic applications. A deeper comprehension of their properties is essential not only for optimizing performance and reliability but also for addressing key challenges in charge transport, polarization dynamics, and leakage mechanisms.

This work aims to make a significant contribution by presenting rigorous methodologies for characterizing dielectric behavior and extracting essential material parameters. By integrating numerical and analytical approaches, it seeks to refine the interpretation of complex dielectric responses, bridging the gap between microscopic charge dynamics and macroscopic observables. Furthermore, the proposed model provides a unified framework for analyzing experimental data, particularly in systems where transport and polarization effects intertwine, such as leaky dielectrics and memristive optoelectronic devices. These insights are expected to enhance predictive capabilities in dielectric spectroscopy and foster innovations in next-generation electronic and photonic technologies.

To achieve these objectives, this research aims to address the following key scientific questions:

- How do nonequilibrium charge dynamics influence dielectric responses in leaky dielectrics?
- What are the fundamental mechanisms behind apparent ferroelectric behavior in non-ferroelectric materials, and how can they be distinguished from genuine ferroelectricity?
- How can advanced impedance and dielectric spectroscopy techniques be used to extract microscopic charge transport parameters?
- What role do leakage currents and charge trapping play in shaping hysteresis loops, and how can their effects be mitigated in practical applications?
- Can the theoretical framework developed for dielectrics be extended to optoelectronic systems, particularly mem-emitters and other devices with memory functionalities?

The main objectives of this master's thesis are as follows:

- Develop a comprehensive theoretical model to describe the influence of nonequilibrium charge carriers on the dielectric response in systems affected by leakage currents and charge trapping mechanisms.
- Generate physically meaningful predictions by selecting appropriate parameters and validating the model against well-established experimental data, ensuring consistency with observed dielectric and impedance responses.
- Identify limitations in traditional impedance spectroscopy and voltammetry techniques by analyzing their capacity to capture nonequilibrium effects, and propose improved experimental protocols for a more complete characterization of dielectric materials.
- Perform a detailed spectral analysis of impedance to extract key transport and polarization parameters, identifying the most suitable equivalent circuit representations based on the theoretical and numerical results.
- Establish correlations between impedance spectroscopy and dielectric permittivity measurements, leading to a unified framework for interpreting polarization dynamics and charge transport in leaky dielectrics.
- Apply the developed model to a case study involving capacitors with memory functionalities, demonstrating its applicability to emerging electronic and optoelectronic devices, including mem-emitters.

By achieving these objectives, this thesis aims to provide deeper insights into the complex interplay between charge dynamics, leakage currents, and polarization responses, offering a valuable framework for both fundamental studies and technological applications.

1.2 Methods

The development of this dissertation involved a comprehensive and systematic approach, integrating theoretical, numerical, and comparative analysis methodologies to construct a robust model for describing nonequilibrium effects in dielectric materials. Thus, in order to establish a solid theoretical foundation, an extensive review of the scientific literature on semiconductor devices and dielectric materials was conducted. This included a thorough examination of both fundamental principles and recent advancements in dielectric and semiconductor physics, ensuring that the proposed model remains consistent with experimental observations and established theories.

A significant part of this work focused on the mathematical formulation of the problem, particularly the study of differential equations governing charge transport, polarization dynamics, and impedance response in leaky dielectrics. Advanced numerical techniques were employed to solve these equations, allowing for the investigation of nonequilibrium effects, leakage currents, saturation phenomena, and frequency-dependent dielectric properties. These numerical simulations provided a detailed and quantitative understanding of the system's behavior under varying conditions.

Furthermore, the theoretical and numerical results were systematically compared with experimental data available in the literature. This validation process ensured the accuracy, reliability, and applicability of the model to real-world dielectric and mem-emitter systems, reinforcing its potential for both fundamental studies and technological applications.

1.3 Dissertation organization

This dissertation is structured into five chapters, followed by bibliographic references and an appendix.

Chapter 1 - **Introduction**. This chapter presents an overview of the main topics covered in this work, outlining the motivation behind the study, the primary objectives, and the methodology employed in its development.

Chapter 2 – **A model for a leaky dielectric**. This chapter is divided into four sections, providing a step-by-step formulation of the theoretical model.

Section 2.1 introduces the polarization transfer function, describing its relation to charge flux and potential barriers within the dielectric.

Section 2.2 presents a statistical framework for charge transport across these potential barriers.

Section 2.3 integrates the previous sections by defining polarization and its fluctuations, leading to expressions for electric displacement, displacement current, and total electric current.

Section 2.4 concludes the chapter by showcasing initial numerical results for polarization and current, illustrating the behavior of the transfer function for both triangular and sinusoidal potentials.

Chapter 3 – **Spectral Analysis**.

Section 3.1 provides an analytical solution for polarization and current up to the second mode under a sinusoidal potential.

Section 3.2 conducts a spectral analysis of current harmonics, extracting conduc-

tance and susceptibility values, which are then used to derive admittance and impedance up to the second mode. An equivalent circuit representation is also introduced.

Section 3.3 extends the impedance analysis by applying a complex potential, leading to the determination of permittivity per mode. The chapter concludes by presenting frequency- and temperature-dependent permittivity graphs, demonstrating the model's ability to describe relaxor-like behavior.

Chapter 4 – **Applications for Mem-Emitter functionalities**. This chapter explores mem-emitters and applies the developed model to these devices, validating its predictions against experimental trends.

Chapter 5 - **Conclusion** The final chapter summarizes the key findings of this work and discusses potential future research directions.

Appendix A The appendix includes a comprehensive table with all parameter values used in generating the figures throughout the dissertation.

2 A Model for a Leaky Dielectric

This chapter provides a comprehensive overview of the general model developed in this work, establishing the foundation for key concepts essential to its understanding. Additionally, it presents the first numerical results obtained from the model's application.

2.1 Polarization Transfer Function

Dielectric materials are classified as insulators due to their limited ability to conduct electricity. Depending on the material's internal structure, charge carriers are not entirely free to move, restricting their displacement within the system. Consequently, when an external electric field is applied, positive charges shift in one direction while negative charges move in the opposite direction, inducing a variation in what is known as the dipole moment [39–41].

If charges are localized within specific sites labeled by an index i, the dipole moment at each site can be defined as

$$p_i = \int \langle r_i \rangle dq_i, \tag{2.1}$$

where $\langle r_i \rangle$ represents the average position of the charge distribution, and dq_i denotes infinitesimal charge variations. Subsequently, in order to describe the macroscopic polarization of the system, the electric polarization P is introduced, defined as the average dipole moment per unit volume, Ω

$$P = \frac{1}{\Omega} \sum_i p_i. \tag{2.2}$$

This quantity characterizes the degree of polarization in the material, reflecting the alignment of dipoles under an external electric field. Note that the polarization P is defined over the total volume Ω of the dielectric, serving as a fundamental parameter in describing its response to external perturbations.

Dielectric materials play a fundamental role in electronic components, particularly in capacitors. A capacitor consists of two conductive plates separated by a distance d, where electric charges accumulate on opposite surfaces when a potential difference is applied, generating an electric field. The region between the plates can be filled with a dielectric material, which prevents the direct flow of electric current while increasing the capacitor's ability to store energy. This enhancement is characterized by an increase in capacitance, denoted as C [42].

In this context, the model proposed in this work considers a capacitor of size d filled with a dielectric material. However, this dielectric is not homogeneous; instead, it

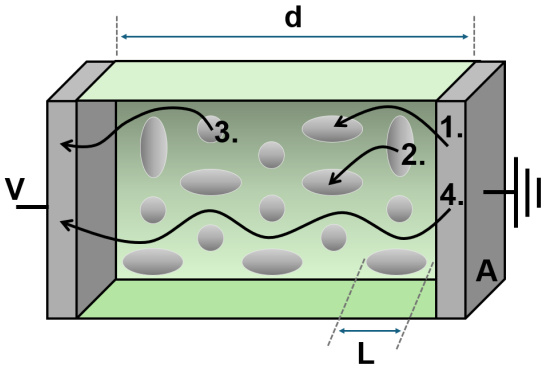

Figure 2 – A representation of a capacitor with a plate separation d and lateral surface area A, filled with a dielectric material with small localization sites of size L. Various paths for the charge dynamics that occur under an applied voltage V are represented by arrows.

consists of multiple small sites of size L. Initially, the charges are in equilibrium, with no dynamics generating currents or fields in the absence of an external potential. Nevertheless, when an external electric field E is applied, each site may respond differently due to its unique internal configuration, which leads to variations in charge distribution within the capacitor and highlights the heterogeneous nature of the material.

Some sites exhibit a higher propensity for charge trapping, while others facilitate charge leakage. These processes introduce local variations in polarization and generate nonequilibrium charge fluctuations, ultimately influencing the overall behavior of the capacitor. The charge dynamics incorporated in this model, illustrated in Figure 2, can be summarized as follows:

1. Charges enter the system and may become trapped within any of the sites.
2. Charges initially localized in one site may escape due to leakage effects and subsequently be captured by another site.
3. Charges may also escape from a site through leakage effects, exiting the system entirely.
4. A small fraction of charges can enter and leave the system directly, bypassing the aforementioned processes.

The displacement of charges from equilibrium due to an applied external electric field can be described by the polarization transfer rate, $\partial P/\partial t\big|^{(\gamma)}$, which governs the temporal evolution of the internal polarization at each site. This phenomenon arises from the cumulative effect of local charge motion, where charges are either generated or trapped. Mathematically, it is expressed as the summation of the time rate of local charge variations, $\partial q_i/\partial t$, occurring at an average position $\langle r_i \rangle$ within a volume $\Omega = d \cdot A$, where A represents

the area of the capacitor plates

$$\left.\frac{\partial P}{\partial t}\right|^{(\gamma)} = \frac{1}{\Omega}\sum_i \frac{\partial q_i}{\partial t}\langle r_i\rangle. \tag{2.3}$$

The index (γ) is introduced in Equation (2.3) to account for its dual applicability, providing a unified mathematical framework to describe both polarization dynamics and leakage effects. Specifically, it applies to the internal polarization of charges when $\gamma = p$ and to the leakage processes occurring at individual sites when $\gamma = lk$. The electric dipole moment, as defined in Equation (2.1), appears in Equation (2.3) through the term $\partial q_i\langle r_i\rangle$, directly influencing the overall behavior of the system by coupling charge motion to polarization dynamics.

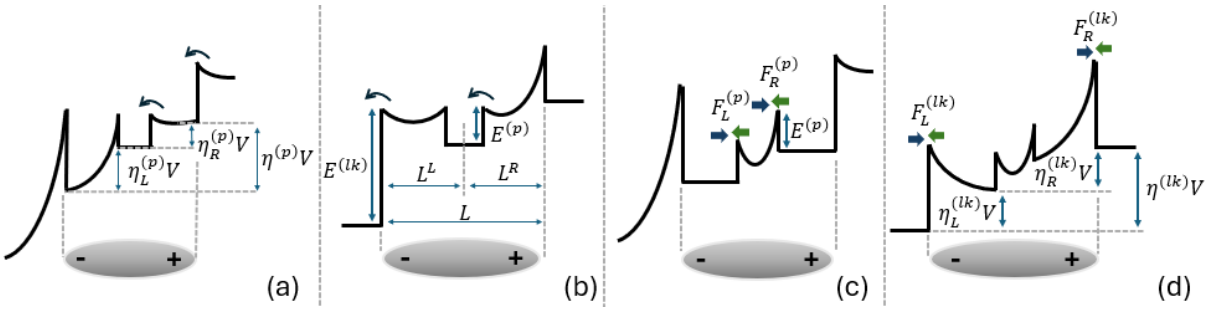

Figure 3 – Band profiles of the charge localization sites along the electric field direction: (a) Band profile describing the local voltage drop distribution within a localization site with both $E^{(p)}$ and $E^{(lk)}$ located in the inner side. (b) Band profile scheme pointing to the relative position of the charge source (trap), with $E^{(p)}$ and $E^{(lk)}$ located in the inner and outer sides, respectively. (c) Band profile showing the carrier fluxes overcoming $E^{(p)}$ barriers that lead to the charge bouncing within the site, with $E^{(p)}$ and $E^{(lk)}$ located in the outer and inner sides, respectively. (d) Band profile showing the carrier fluxes overcoming $E^{(lk)}$ barriers that lead to the charge leak, with both $E^{(p)}$ and $E^{(lk)}$ located in the outer side.

The summation in Equation (2.3) can be reformulated to emphasize the contributions from charge fluctuations within sites aligned in planes indexed by k, as well as the influence of charge distribution on polarization dynamics along the direction perpendicular to the capacitor plates, indexed by j. Additionally, the expression can be rewritten in terms of the capacitor's area A and distance d

$$\left.\frac{\partial P}{\partial t}\right|^{(\gamma)} = \frac{1}{d}\sum_j \frac{1}{A}\sum_k \frac{\partial q_j^{(k)}}{\partial t}\langle r_j\rangle. \tag{2.4}$$

A portion of Equation (2.4) represents the charge flux across both internal and external barriers of the sites, denoted as $F_j^{(\lambda)} \equiv (1/A)\sum_k(\partial q_j^{(k)}/\partial t)$. Consequently, Equation (2.4) can be rewritten as:

$$\left.\frac{\partial P}{\partial t}\right|^{(\gamma)} = \frac{1}{d}\sum_j F_j^{(\gamma)}\langle r_j\rangle. \tag{2.5}$$

Considering the capacitor illustrated in Figure 2, in the case of a uniform site distribution, the parameter η represents the inverse of the number of sites between the

two contacts. It is defined as the ratio of the site size L to the capacitor size d

$$\eta = \frac{L}{d}. \tag{2.6}$$

Furthermore, each site experiences a fraction of the applied voltage V proportional to ηV, which leads to η being referred to as the voltage drop efficiency per site, or simply efficiency. Figure 3 presents four geometric representations (a-d) that illustrate distinct energy site profiles associated with different efficiency values η. These diagrams qualitatively depict charge trapping and leakage dynamics. While they do not encompass all possible configurations, they provide valuable insights into the fundamental charge transport mechanisms governing the system. The inner well represents the source or trap of non-equilibrium carriers, delimited by a potential barrier $E^{(p)}$ that must be overcome for dipoles to be generated within the localization site of size L. These localized charges can oscillate within the site, confined by the barriers $E^{(lk)}$. Leakage processes occur through these barriers.

Figure 3(a) depicts a system with a strong tendency to store charges, whereas Figure 3(b) illustrates an escape profile, highlighting the disparity in external barrier energies, $E^{(lk)}$, between the two systems, which differ from the internal barrier energy, $E^{(p)}$. In Figure 3(a), the total efficiency η can be decomposed into two components, expressed as $\eta = \eta_L + \eta_R$, exhibiting an intrinsic energy asymmetry. This asymmetry is introduced through the parameter $\alpha \in [0, \infty]$, where

$$\eta_L = \frac{\alpha\eta}{1+\alpha}, \quad \eta_R = \frac{\eta}{1+\alpha}, \tag{2.7}$$

with the symmetric case occurring when $\alpha = 1$. Furthermore, the processes of charge trapping and generation may eventually saturate, affecting the polarization fluctuation term in Equation (2.3) at higher voltages. This saturation phenomenon occurs exclusively in polarization transfer, $\partial P/\partial t\big|^{(p)}$, where efficiency is modified as follows

$$\eta \to \frac{\eta}{\sqrt{1+\beta V^2}}, \tag{2.8}$$

where β is the saturation coefficient. Similarly, spatial asymmetry within the sites can also arise, as illustrated in Figure 3(b). In this case, the left-side region is defined as $L_L = \alpha L/(1+\alpha)$, while the right-side region is given by $L_R = L/(1+\alpha)$, satisfying the total site size condition $L = L_L + L_R$.

Figures 3(c) and 3(d) illustrate scenarios where charge flux occurs across both internal and external barriers but remains unidirectional, either towards the left or the right. Consequently, the summation terms in Equation (2.5) simplify to a sum of the flux-distance products,

$$F_L^{(\gamma)} L_L + F_R^{(\gamma)} L_R, \tag{2.9}$$

accounting for contributions from both sides. Additionally, the number of site locations, expressed as the inverse of Equation (2.6) per charge unit q, ultimately leads to the following expression for the polarization transfer function in Equation (2.5)

$$\left.\frac{\partial P}{\partial t}\right|^{(\gamma)} = \frac{q}{d\eta}\left(F_L^{(\gamma)} L_L + F_R^{(\gamma)} L_R\right). \tag{2.10}$$

2.2 Fluxes of charges

The fluxes in Equation (2.10), $F_L^{(\gamma)}$ and $F_R^{(\gamma)}$, occurring on each side of the localization site, as depicted in Figures 3(c) and 3(d), describe the movement of charges influenced by both local conditions and the applied electric field. These fluxes represent the transport of thermally distributed particles [34], governed by Maxwell-Boltzmann and Fermi-Dirac distributions [43], across the potential barriers. The flux can be defined as the product of the thermal velocity of the particles, $\langle v \rangle$, and the charge density, which corresponds to the number of particles per unit volume, n,

$$F_j^{(\gamma)} = n\langle v \rangle. \tag{2.11}$$

Here, the index j differentiates the side on which the flux occurs, where $j = L$ represents the left side and $j = R$ the right side. The thermal velocity $\langle v \rangle$ can be determined from the following equation

$$\langle v \rangle = \int_0^{\infty}\int_0^{\pi/2}\int_0^{2\pi} \sin(\theta)\cos(\theta)\left(\frac{m^*}{2\pi k_B T_{eff}}\right)^{3/2} v^3 \exp\left(\frac{-m^* v^2}{2k_B T_{eff}}\right) d\phi d\theta dv, \tag{2.12}$$

with m^* representing the effective mass, k_B is the Boltzmann constant [44] and T_{eff} denotes the system's effective temperature [45]. Solving the integrals over $d\phi$ and $d\theta$ is straightforward, $\int_0^{\pi/2} \sin(\theta)\cos(\theta) d\theta = 1/2$ and $\int_0^{2\pi} d\phi = 2\pi$, simplifying the expression for the average thermal velocity of the particles in equation (2.12) to:

$$\langle v \rangle = \pi\left(\frac{m^*}{2\pi k_B T_e f f}\right)^{3/2} \int_0^{\infty} v^3 \exp\left(-\frac{m^* v^2}{2k_B T_{eff}}\right) dv. \tag{2.13}$$

For simplicity, the constants can be grouped into $\zeta = m^*/(2k_B T_{eff})$, reducing the integral in equation (2.13) to the following compact expression

$$J = \int_0^{\infty} v^3 e^{-\zeta v^2} dv = \int_0^{\infty} v^2 e^{-\zeta v^2} v dv. \tag{2.14}$$

Thus, equation (2.14) is now transformed into a Gaussian integral, which can be readily solved by substituting $z = \zeta v^2$ and $dz = 2\zeta v dv$. This transformation simplifies the integral, allowing the solution to be obtained using the method of integration by parts

$$J = \frac{1}{2\zeta^2}\int_0^{\infty} z e^{-z} dz = \frac{1}{2\zeta^2}. \tag{2.15}$$

Subsequently, the thermal velocity $\langle v \rangle$ of the charges in (2.13) is finally determined by incorporating the result obtained above (2.15), along with the constant ζ, yielding

$$\langle v \rangle = 2\pi \left(\frac{m^*}{2\pi k_B T_{eff}} \right)^{3/2} \left(\frac{k_B T_{eff}}{m^*} \right)^2 = \left(\frac{k_B T_{eff}}{2\pi m^*} \right)^{1/2}. \tag{2.16}$$

The number of charges per unit volume, n, in Equation (2.11), assuming trapped Fermions, is given by [43]

$$n = \int_{E_0}^{\infty} D(E) f_{FD}(E, \mu) dE, \tag{2.17}$$

where μ is the local chemical potential, $D(E)$ is the density of states, defined as

$$D(E) = \frac{m^*}{\pi^2 \hbar^3} \sqrt{2m^*(E - E^{(\gamma)})}, \tag{2.18}$$

and $f_{FD}(E, \mu)$ is the Fermi-Dirac distribution, given by

$$f_{FD}(E, \mu) = \frac{1}{1 + \exp\left(\frac{E - \mu_j}{k_B T_{eff}}\right)}. \tag{2.19}$$

Thus, substituting these definitions into Equation (2.17), the charge density can be expressed as

$$n = \frac{m^* \sqrt{2m^*}}{\pi^2 \hbar^3} \int_{E_0 = E^{(\gamma)}}^{E + \infty} \frac{(E - E^{(\gamma)})^{1/2}}{1 + \exp\left(\frac{E - \mu_j}{k_B T_{eff}}\right)} dE. \tag{2.20}$$

To simplify the integral in Equation (2.20), we introduce the following substitutions:

$$x = \frac{E - E^{(\gamma)}}{k_B T_{eff}}, \tag{2.21}$$

$$\xi = \frac{-(E^{(\gamma)} - \mu_j)}{k_B T_{eff}}. \tag{2.22}$$

Additionally, assuming a nondegenerate electron gas, where $\exp(x - \xi) \gg 1$ and $\left(\frac{E - \mu}{k_B T_{eff}}\right) \gg 1$, we define a grouping constant:

$$\rho = \frac{\sqrt{2}(m^* k_B T_{eff})^{3/2}}{\pi^2 \hbar^3}. \tag{2.23}$$

Applying these substitutions, Equation (2.20) simplifies to

$$n = \rho e^{\xi} \int_0^{\infty} x^{1/2} e^{-x} dx. \tag{2.24}$$

Using the transformation $x = z^2$ with $dx = 2z dz$, we recognize the integral as a Gaussian integral, yielding

$$n = 2\rho e^{\xi} \int_0^{\infty} z^2 e^{-z^2} dz = \frac{\sqrt{\pi}}{2} \rho e^{\xi}. \tag{2.25}$$

Substituting Equation (2.25) back into Equation (2.24), we obtain the final expression for the charge density:

$$n = \frac{1}{\sqrt{2}} \left(\frac{m^* k_B T_{eff}}{\pi \hbar^2} \right)^{3/2} \exp\left(\frac{-E^{(\gamma)} + \mu_j}{k_B T_{eff}} \right). \tag{2.26}$$

The charge flux in a specific direction is then obtained by substituting the velocity from Equation (2.16) and the charge density from Equation (2.26) into Equation (2.11):

$$F_j^{(\gamma)} = \frac{4\pi m^*}{(2\pi\hbar)^3}(k_B T_{eff})^2 \exp\left(\frac{-E^{(\gamma)} + \mu_j}{k_B T_{eff}}\right). \tag{2.27}$$

Then, the net flux through each barrier comprises fluxes in opposite directions. By combining these fluxes using Equation (2.27) and considering the band profiles illustrated in Figure 3, the flux expressions as a function of the applied voltage are obtained:

$$F_{L(R)}^{(\gamma)} = \pm\lambda^{(\gamma)}\left[1 - \exp\left(\mp\eta_{L(R)}\frac{eV}{k_B T_{eff}}\right)\right], \tag{2.28}$$

$$F_{R(L)}^{(\gamma)} = \pm\lambda^{(\gamma)}\left[\exp\left(\mp\eta_{R(L)}\frac{eV}{k_B T_{eff}}\right) - 1\right], \tag{2.29}$$

where the subscripts L and R indicate the left and right barriers, respectively. The parameter $\lambda^{(\gamma)}$ in Equation (2.28) is defined as

$$\lambda^{(\gamma)} = \frac{4\pi m^*}{(2\pi\hbar)^3}(k_B T_{eff})^2 \exp\left(-\frac{E^{(\gamma)}}{k_B T_{eff}}\right). \tag{2.30}$$

The choice of signs in Equations (2.28) and (2.29) depends on the band profile and determines the character of the polarization transfer function in Equation (2.10).

2.3 Fluctuations in polarization and current

The polarization within the dielectric, as defined in Equation (2.2), can be further characterized in this approach by the combination of the following components

$$P = P_\infty + \delta P^{(p)} - \delta P^{(lk)}. \tag{2.31}$$

The first term in Equation (2.31), P_∞, represents the instantaneous polarization, which is directly related to the electric field E as:

$$P_\infty = \varepsilon_0 \chi_\infty E. \tag{2.32}$$

Here, ε_0 is the permittivity of vacuum, and χ_∞ is the instantaneous electric susceptibility, an inherent material property. The total electric field E in the system, which includes contributions from internal fields generated by the dielectric [46], is given in terms of the applied potential as

$$E = \frac{V}{d}. \tag{2.33}$$

The remaining terms in Equation (2.31), $\delta P^{(p)}$ and $\delta P^{(lk)}$, represent fluctuations in polarization around an equilibrium point due to non-equilibrium charge fluctuations within the

localization site and leakage, respectively. These fluctuations are governed by the following differential equation, which describes their evolution over the relaxation time $\tau^{(\gamma)}$

$$\frac{d\delta P^{(\gamma)}}{dt} = -\frac{\delta P^{(\gamma)}}{\tau^{(\gamma)}} + \left.\frac{\partial P}{\partial t}\right|^{(\gamma)}. \tag{2.34}$$

Notably, in Equation (2.31), the index γ reappears, as the solutions for polarization fluctuations (2.10), both internal and leakage-related, follow analogous patterns. The internal polarization fluctuation, $\delta P^{(p)}$, is initially positive, meaning its contribution to total polarization retains the same sign as its result. In contrast, the leakage fluctuation, $\delta P^{(lk)}$, assumes a negative sign, exerting an opposing effect. Moreover, because the relaxation time $\tau^{(\gamma)}$ is present in both scenarios, significant contrast between them may emphasize one effect over the other. The extent to which one effect becomes more prominent critically depends on how closely the speed of the external drive matches the relevant relaxation time.

The term $\partial P/\partial t|^{(\gamma)}$ in Equation (2.34) corresponds to the polarization transfer function appearing in Equation (2.10), incorporating the charge fluxes from Equations (2.28) and (2.29).

Another fundamental quantity relating the electric field to polarization in a dielectric material is the electric displacement field [39, 46]

$$\mathbf{D} = \varepsilon_0 \mathbf{E} + \mathbf{P}. \tag{2.35}$$

Taking the time derivative of $\mathbf{D}$ yields the displacement current j_D

$$\mathbf{j}_D = \varepsilon_0 \frac{d\mathbf{E}}{dt} + \frac{d\mathbf{P}}{dt}. \tag{2.36}$$

Substituting Equations (2.31), (2.32), and (2.33) into the displacement current expression (2.36) results in

$$j_D = \frac{\varepsilon_0}{d}\frac{dV}{dt} + \frac{\varepsilon_0 \chi_\infty}{d}\frac{dV}{dt} + \frac{d\delta P^{(p)}}{dt} - \frac{d\delta P^{(lk)}}{dt}. \tag{2.37}$$

The total current I can be expressed in terms of the displacement current (2.37), with an additional conductance term G_0 and nonequilibrium charge fluctuation δn [34,47,48]

$$I = j_D \cdot A + (G_0 + \Gamma \delta n)\, V. \tag{2.38}$$

where $\Gamma = e\mu/d^2$, with μ representing the mobility of out-of-equilibrium charges. In this model, it is assumed that $G_0 \gg \Gamma \delta n$. Expanding the displacement current terms, the capacitance naturally emerges in Equation (2.37), defined as:

$$C = \varepsilon_0 (1 + \chi_\infty)\frac{A}{d}. \tag{2.39}$$

Thus, substituting Equation (2.39) into Equation (2.38), the total current can be rewritten in terms of the capacitance C, the electric potential V, and polarization fluctuations $\delta P^{(\gamma)}$

$$I = C\frac{dV}{dt} + A \cdot \left(\frac{d\delta P^{(p)}}{dt} - \frac{d\delta P^{(lk)}}{dt} \right) + G_0 V. \tag{2.40}$$

2.4 Graphical analysis and initial results

With the expressions for the polarization transfer function (2.3), polarization (2.31), and current (2.40) established, the next step is to determine the appropriate form of the applied potential V and the correct parameters to generate meaningful results that align with reality. However, depending on the choice of parameters and the form of the applied potential V in certain types of problems, finding an analytical solution becomes unlikely. The presence of a nonzero saturation term β further complicates the situation. Consequently, solving the ordinary differential equation (2.34) numerically is straightforward using methods like the 4th-order Runge-Kutta.

The first potential considered is a triangular waveform, commonly used in various physical systems [49, 50]. As shown in Figure 4(a), this waveform starts at zero, increases linearly to its maximum amplitude, and then symmetrically decreases to the same amplitude on the negative side, forming distinct triangular peaks and valleys.

Figure 4(b) illustrates the polarization transfer functions in the absence of leakage effects. In systems where saturation occurs ($\beta \neq 0$, solid lines), the curves converge to a specific value beyond a certain voltage threshold. This behavior contrasts with non-saturated systems ($\beta = 0$, dashed lines), where the response exhibits a monotonic growth, following the voltage polarity. In asymmetric cases, the transfer function diverges toward the negative side when $\alpha < 1$, toward the positive side when $\alpha > 1$, and symmetrically in both directions when $\alpha = 1$. Panel 4(c) presents the corresponding polarization curves, where a mirroring effect is evident between opposite quadrants, as well as between the curves with asymmetries $\alpha = 10^2$ and $\alpha = 10^{-2}$. Furthermore, at zero voltage, the polarization retains a nonzero value, and the curves exhibit a counterclockwise trajectory, reminiscent of the hysteresis loops observed in ferroelectric materials [51–53]. The respective current responses, displayed in panel 4(d), reveal that for $\alpha = 10^2$ and $\alpha = 10^{-2}$, the extrema shift above and below the symmetric case $\alpha = 1$ (blue curve). Despite minor shifts, all curves exhibit a clockwise orientation.

The second row, panels 4(e–g), showcases the polarization transfer functions along with their respective polarization and current responses, still without leakage effects. In this scenario, only the efficiency parameter η varies, while all other parameters remain constant. A noticeable trend is that the maxima and minima of each curve progressively increase with efficiency. Panel 4(f) demonstrates that the polarization curves maintain a counterclockwise trajectory, as seen in panel 4(c). However, they exhibit a pronounced

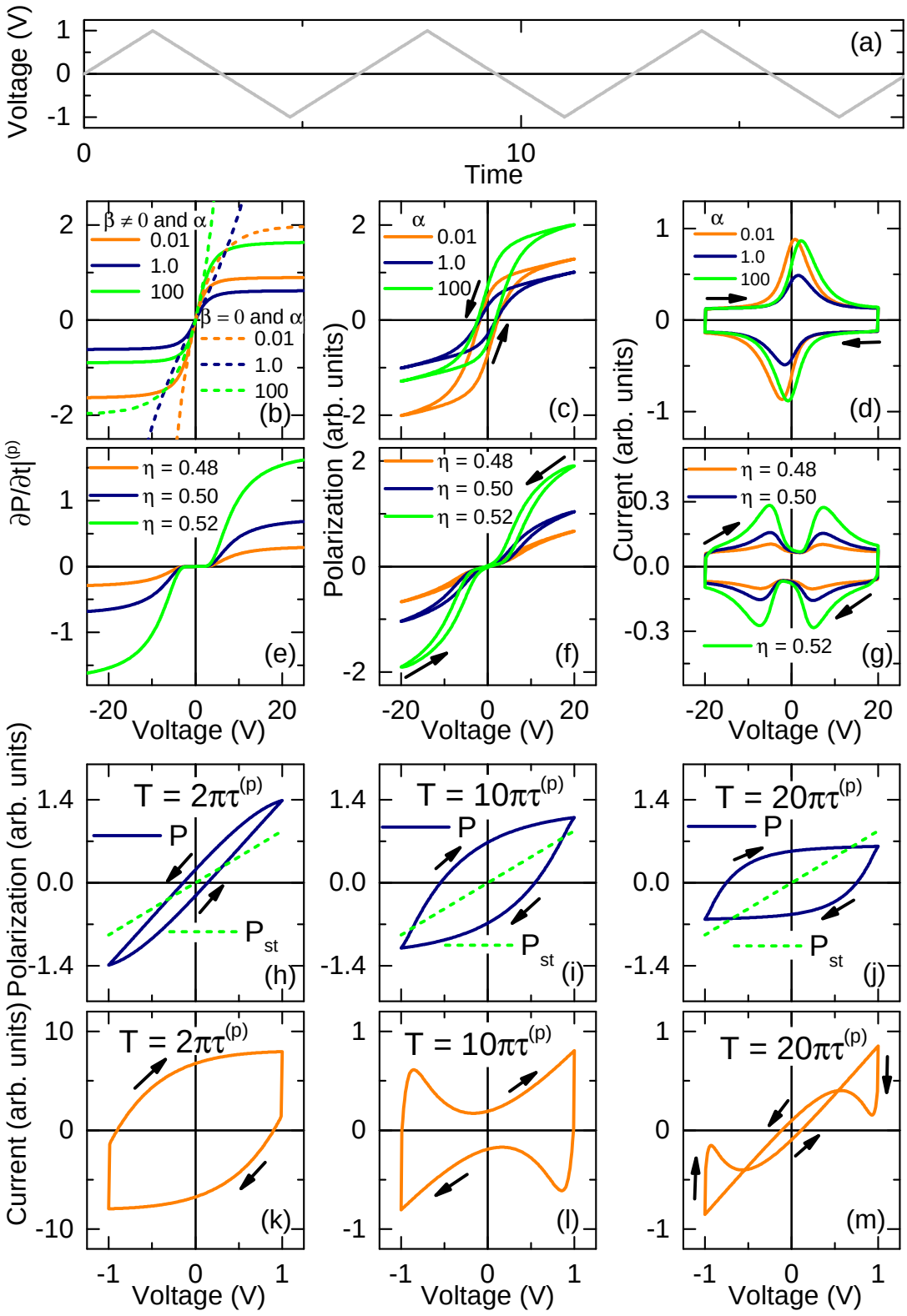

Figure 4 – (a) Triangular voltage drive. Without leakage effects: (b) Transfer functions for varying asymmetry α and saturation β, (c) the corresponding polarizations P and (d) currents I. (e) Transfer functions for varying efficiency, η, (f) the corresponding polarizations P and (g) currents I. With leakage effects: (h-j) Calculated polarization P as a function of voltage along with the stationary states P_{st} plotted as dashed curves. (k-l) The corresponding calculated currents I. The parameters are detailed in Table 1 of Appendix A.

narrowing of the hysteresis loops near zero voltage. This effect arises from the substantially higher efficiency value, 100 times greater than that used in the upper row—resulting in a system response that resembles a double hysteresis loop, a feature often associated with antiferroelectric behavior [54–57]. The currents in panel 4(g) continue to display clockwise behavior.

The third and fourth rows, Figures 4(h–m), correspond to the polarization P, stationary states P_{st}, and currents I influenced by leakage effects, while varying only the period of the sweep voltage, T. In these cases, saturation effects are neglected, with $\beta \approx 0$, leading to interesting outcomes where the voltage amplitude V is significantly smaller compared to the previous cases. Notably, the polarization in panel 4(h) follows a counterclockwise trajectory, remains nonzero at $V = 0$, and is associated with a clockwise current in panel 4(k). This behavior mirrors the observations in panels 4(c) and 4(d) for a sweep voltage period of $T = 2\pi\tau^{(p)}$ and a time ratio of $10\tau^{(p)} = \tau^{(lk)}$. However, when the sweep voltage period is increased to $T = 10\pi\tau^{(p)}$ and the ratio to $5\tau^{(p)} = \tau^{(lk)}$, the polarization in panel 4(i) reverses to a clockwise direction. This inversion is caused by an increased contribution from leakage effects, which dissipate the polarization created by trapped charges. Essentially, the system becomes unable to sustain the accumulated polarization.

These inverted hysteresis loops are referred to as *proteresis* in the literature [58–60], a term derived from the Greek meaning "what comes before," as these cycles appear to anticipate the response. Conversely, the term hysteresis literally means "what comes after," representing the opposite effect [61]. However, the model proposed in this work is not associated with the timing of the dynamics but rather with the nature of the transfer function, which dictates the trapping and release of charge carriers. For this reason, the term "inverted hysteresis" remains an accurate and appropriate description. Meanwhile, the current in panel 4(l) retains its clockwise direction.

Further increasing the period to $T = 20\pi\tau^{(p)}$ and the ratio to $\tau^{(p)} = \tau^{(lk)}$, the polarization in panel 4(j) continues to follow a clockwise trajectory. However, the current in panel 4(m) undergoes a directional change, crossing at two points and exhibiting counterclockwise behavior during certain phases of its dynamics. This phenomenon is associated with the detrapping of electrons that were previously confined. Both the inversion of polarization and current curves have been experimentally observed, further validating the applicability of this model [62,63]. Over even longer periods, we observe the narrowing of the current-voltage loop.

To contrast the results obtained with a triangular voltage drive in Figure 4, a sinusoidal potential is applied to the model, leading to the results shown in Figure 5, where the same parameters are used. As illustrated in panel 5(a), the most noticeable difference is that the function does not start at the origin but rather at its maximum amplitude,

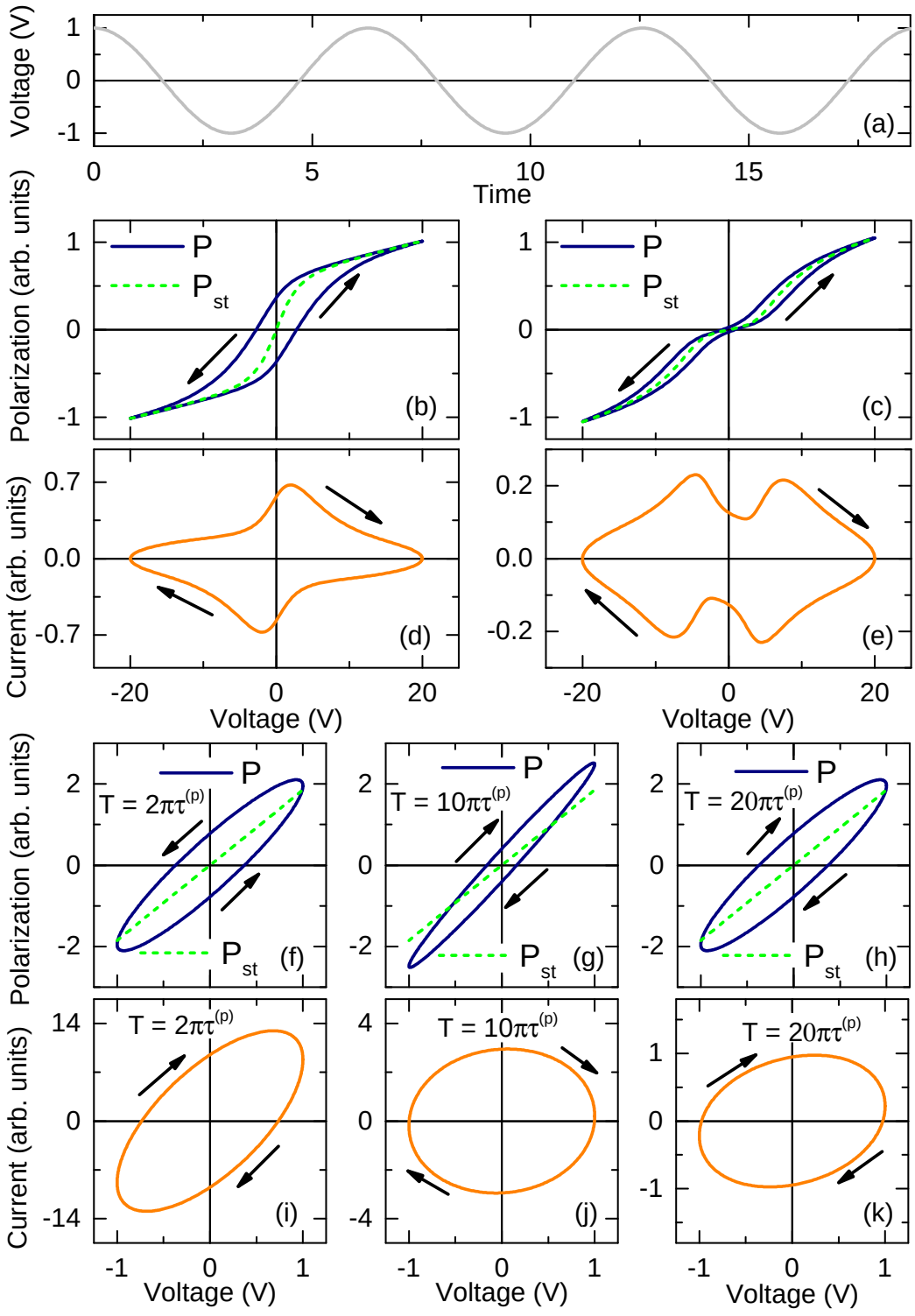

Figure 5 – (a) Sinusoidal voltage drive. (b-c) Calculated polarizations P as a function of applied voltage, the stationary state P_{st} are protted using dashed curves. (d-e) Calculated corresponding currents I, in absence of leakage. (f-h) Calculated polarization as a function of voltage and their stationary states P_{st} in presence of leakage and (i-k) the corresponding currents I for various period, T, values. The parameters are detailed in Table 1 of Appendix A.

as it follows a cosine waveform. The polarization curves, shown in panels 5(b) and 5(c), along with their corresponding current responses in panels 5(d) and 5(e), represent the case without leakage effects. The resulting curves closely resemble the symmetric cases presented in Figure 4 and follow the same directional behavior.

The most significant differences arise in the polarization and current curves when leakage effects are introduced, particularly at low potential amplitudes V, where they exhibit elliptical shapes. In the polarization plots, depicted in panels 5(f–h), the same directional reversal observed in Figure 4 occurs as the period T increases, transitioning to a clockwise orientation for $T = 10\pi\tau^{(p)}$. Additionally, caution must be exercised when interpreting the ferroelectric nature of such polarization curves, as emphasized in reference 25, where even a banana skin can exhibit a polarization ellipse. Meanwhile, the current responses, shown in panels 5(i–k), consistently maintain a clockwise direction, even as the period T increases.

3 Spectral Analysis

This chapter provides an analytical solution for the polarization and current described in the model, along with a detailed analysis of impedance and dielectric spectroscopy and their implications.

3.1 Analytical solutions to polarization and current

Analytical solutions to the differential equation (2.34) can be derived depending on the specific property being investigated. In this work, two approaches are developed, both aimed at determining key parameters that ultimately interconnect. Impedance spectroscopy [64,65] provides impedance values, characterizing the resistivity of an electrical circuit as a whole. In contrast, dielectric spectroscopy [66, 67] measures the complex permittivity of a material as a function of frequency. The complex permittivity quantifies the material's response to an applied electric field, encompassing both the storage and dissipation of electrical energy. It reflects the polarization mechanisms within the material, which arise from the interactions between the applied field and the constituent charges (e.g., electronic, ionic, dipolar). The complex permittivity exhibits significant dependence on frequency ω and effective temperature T_{eff}.

For impedance spectroscopy, an analytical solution can be obtained depending on the type of potential applied to the system, by neglecting the saturation term β, which appears in the efficiency expression (2.8). Thus, we will assume $\beta \to 0$, which is valid in the small amplitude approximation. A sinusoidal potential, or AC voltage, such as the one used to generate the results in Figure 5, is well suited for this analysis

$$V(t) = V_0 \cos(\omega t). \tag{3.1}$$

By applying this potential (3.1) to the fluxes (2.28) and (2.29), choosing the upper signs, and subsequently to the polarization transfer function (2.10), the following explicit expression for the polarization fluctuation (2.34) is obtained. The equations for internal polarization (p) and leakage (lk) follow a similar structure

$$\frac{d\delta P^{(\gamma)}(t)}{dt} = -\frac{\delta P^{(\gamma)}(t)}{\tau^{(\gamma)}} + \frac{e\lambda^{(\gamma)}L}{d\eta(\alpha+1)}\Bigg\{\alpha - \alpha \exp\left[\frac{\alpha}{(\alpha+1)}\left(\frac{eV_0}{k_B T_{eff}}\right)\cos(\omega t)\right] + \exp\left[\frac{1}{(\alpha+1)}\left(\frac{eV_0}{k_B T_{eff}}\right)\cos(\omega t)\right] - 1\Bigg\}. \tag{3.2}$$

The spectral analysis is typically performed using small amplitude signals. This allows us to approximate the arguments inside the exponential terms as small, i.e., $eV_0/(k_B T_{eff}) \ll 1$,

enabling a series expansion up to the second order. After algebraic simplifications, the expression reduces to

$$\frac{d\delta P^{(\gamma)}(t)}{dt} = -\frac{\delta P^{(\gamma)}(t)}{\tau^{(\gamma)}} + e\lambda^{(\gamma)}\frac{(\alpha^2+1)}{(\alpha+1)}\frac{\eta eV_0}{k_BT_{eff}}\cos(\omega t) + \frac{e\lambda^{(\gamma)}}{2}\frac{(\alpha^3-1)}{(\alpha+1)^2}\left(\frac{\eta eV_0}{k_BT_{eff}}\right)^2\cos^2(\omega t). \quad (3.3)$$

To simplify the solution of the differential equation above, the time-independent constants are grouped into the following expressions

$$\sigma_1^{(\gamma)} = e\lambda^{(\gamma)}\frac{(\alpha^2+1)}{(1+\alpha)^2}\frac{\eta eV_0}{k_BT_{eff}} \quad (3.4)$$

$$\sigma_2^{(\gamma)} = \frac{e\lambda^{(\gamma)}}{2}\frac{(\alpha^3-1)}{(1+\alpha)^3}\left(\frac{\eta eV_0}{k_BT_{eff}}\right)^2 \quad (3.5)$$

In symmetric systems, where $\alpha = 1$, the term $\sigma_2^{(\gamma)}$ vanishes due to the operation in the numerator. Additionally, using the trigonometric identity $\cos^2(\omega t) = 1/2+[\cos(2\omega t)]/2$, the differential equation (3.3) simplifies further to

$$\frac{d\delta P^{(\gamma)}(t)}{dt} = -\frac{\delta P^{(\gamma)}(t)}{\tau^{(\gamma)}} + \sigma_1^{(\gamma)}\cos(\omega t) + \frac{\sigma_2^{(\gamma)}}{2}\cos(2\omega t) + \frac{\sigma_2^{(\gamma)}}{2}. \quad (3.6)$$

To solve this equation for polarization fluctuations, the Laplace transform method [68] is applied. Each term is individually transformed, converting time dependence t into frequency dependence s

$$\mathcal{L}\left\{\frac{d\delta P^{(\gamma)}(t)}{dt}\right\} = -\delta P^{(\gamma)}(0) + s\Pi^{(\lambda)}(s) \quad (3.7)$$

$$\mathcal{L}\{\delta P^{(\gamma)}(t)\} = \Pi^{(\gamma)}(s) \quad (3.8)$$

$$\mathcal{L}\{1\} = \frac{1}{s} \quad (3.9)$$

$$\mathcal{L}\{\cos(n\omega t)\} = \frac{s}{s^2+(n\omega)^2}. \quad (3.10)$$

Applying the Laplace transform to Equation (3.6), substituting the results from the above expressions, and isolating the frequency-dependent function $\Pi^{(\lambda)}(s)$, we obtain

$$\Pi^{(\lambda)}(s) = \frac{\delta P^{(\gamma)}(0)}{(s+1/\tau^{(\gamma)})} + \sigma_1^{(\gamma)}\frac{s}{(s^2+\omega^2)}\frac{1}{(s+1/\tau^{(\gamma)})} + \frac{\sigma_2^{(\gamma)}}{2}\frac{s}{(s^2+4\omega^2)}\frac{1}{(s+1/\tau^{(\gamma)})} + \frac{\sigma_2^{(\gamma)}}{2}\frac{1}{s(s+1/\tau^{(\gamma)})}. \quad (3.11)$$

To recover the time-dependent function, in this case, the polarization fluctuation $\delta P^{(\gamma)}(t)$, the inverse Laplace transform is applied to each term in Equation (3.11). The resulting

expressions provide a complete analytical solution for the time evolution of polarization fluctuations

$$\mathcal{L}^{-1}\{\Pi^{(\lambda)}(s)\} = \delta P^{(\lambda)}(t) \tag{3.12}$$

$$\mathcal{L}^{-1}\{(s+1/\tau)\} = e^{-t/\tau} \tag{3.13}$$

$$\mathcal{L}^{-1}\left\{\frac{1}{s(s+1/\tau)}\right\} = \tau - \tau e^{-t/\tau} \tag{3.14}$$

$$\mathcal{L}^{-1}\left\{\frac{1}{[s^2+(n\omega)^2](s+1/\tau)}\right\} = \frac{\tau\cos(n\omega t)}{1+(n\omega\tau)^2} + \frac{n\omega\tau^2\sin(n\omega\tau)}{1+(n\omega\tau)^2} - \frac{\tau e^{-t/\tau}}{1+(n\omega\tau)^2} \tag{3.15}$$

The final result, given by Equation (3.15), holds for $n = 1, 2$ in this case. Therefore, applying the inverse Laplace transform to Equation (3.11) and substituting the obtained results, the final expression for the fluctuation in polarization, $\delta P(t)$, is determined as

$$\begin{aligned}\delta P^{(\gamma)}(t) = f_0 e^{-t/\tau^{(\gamma)}} &+ \frac{\sigma_1^{(\gamma)}\tau^{(\gamma)}}{1+(\omega\tau^{(\gamma)})^2}\left[\cos(\omega t) + \omega\tau^{(\gamma)}\sin(\omega t)\right] \\ &+ \frac{\sigma_2^{(\gamma)}\tau^{(\gamma)}}{2[1+(2\omega\tau^{(\gamma)})^2]}\left[\cos(2\omega t) + 2\omega\tau^{(\gamma)}\sin(2\omega t)\right] + \frac{\sigma_2^{(\gamma)}\tau^{(\gamma)}}{2},\end{aligned} \tag{3.16}$$

where the term f_0 is defined as

$$f_0 = \delta P(0) - \frac{\sigma_1^{(\gamma)}\tau^{(\gamma)}}{1+(\omega\tau^{(\gamma)})^2} - \frac{\sigma_2^{(\gamma)}\tau^{(\gamma)}}{2[1+(2\omega\tau^{(\gamma)})^2]} - \frac{\sigma_2^{(\gamma)}\tau^{(\gamma)}}{2} \tag{3.17}$$

This grouping is performed because the exponential term associated with f_0 in Equation (3.16) decays to zero over time, as $\lim_{t\to\infty} e^{-t/\tau^{(\gamma)}} = 0$. Substituting the respective fluctuations from both the internal polarization, $\delta P^{(p)}(t)$, and the leakage contribution, $\delta P^{(lk)}(t)$, into Equation (2.31) yields the total polarization $P(t)$

$$\begin{aligned}P(t) = \varepsilon_0\chi_\infty\frac{V_0}{d}\cos(\omega t) &+ \frac{\sigma_1^{(p)}\tau^{(p)}}{1+(\omega\tau^{(p)})^2}\left[\cos(\omega t) + \omega\tau^{(p)}\sin(\omega t)\right] \\ &+ \frac{\sigma_2^{(p)}\tau^{(p)}}{2[1+(2\omega\tau^{(p)})^2]}\left[\cos(2\omega t) + 2\omega\tau^{(p)}\sin(2\omega t)\right] + \frac{\sigma_2^{(p)}\tau^{(p)}}{2} \\ &- \frac{\sigma_1^{(lk)}\tau^{(lk)}}{1+(\omega\tau^{(lk)})^2}\left[\cos(\omega t) + \omega\tau^{(lk)}\sin(\omega t)\right] \\ &- \frac{\sigma_2^{(lk)}\tau^{(lk)}}{2[1+(2\omega\tau^{(lk)})^2]}\left[\cos(2\omega t) + 2\omega\tau^{(lk)}\sin(2\omega t)\right] - \frac{\sigma_2^{(lk)}\tau^{(lk)}}{2}.\end{aligned} \tag{3.18}$$

Applying a sinusoidal potential (3.1) to the current expression (2.40), the equation above can be differentiated with respect to time to express it in terms of the displacement current (2.36). This results in the following expression for the total current, with terms

associated with the sine and cosine components grouped accordingly

$$
\begin{aligned}
I(t) = V_0 \left\{ \frac{A}{V_0} \left[\frac{\sigma_1^{(p)} (\omega\tau^{(p)})^2}{1+(\omega\tau^{(p)})^2} - \frac{\sigma_1^{(lk)} (\omega\tau^{(lk)})^2}{1+(\omega\tau^{(lk)})^2} \right] + G_0 \right\} \cos(\omega t) \\
+ V_0 \left\{ \frac{A}{V_0} \left[\frac{\sigma_1^{(p)} \omega\tau^{(p)}}{1+(\omega\tau^{(p)})^2} - \frac{\sigma_1^{(lk)} \omega\tau^{(lk)}}{1+(\omega\tau^{(lk)})^2} \right] + \omega C \right\} \sin(\omega t) \\
+ V_0 \left\{ \frac{2A}{V_0} \left[\frac{\sigma_2^{(p)} (\omega\tau^{(p)})^2}{1+(\omega\tau^{(p)})^2} - \frac{\sigma_2^{(lk)} (\omega\tau^{(lk)})^2}{1+(\omega\tau^{(lk)})^2} \right] \right\} \cos(2\omega t) \\
+ V_0 \left\{ \frac{A}{V_0} \left[\frac{\sigma_2^{(p)} \omega\tau^{(p)}}{1+(\omega\tau^{(p)})^2} - \frac{\sigma_2^{(lk)} \omega\tau^{(lk)}}{1+(\omega\tau^{(lk)})^2} \right] \right\} \sin(2\omega t). \quad (3.19)
\end{aligned}
$$

3.2 Impedance spectroscopy

Upon analyzing the total current derived in the previous section, as described by Equation (3.19), it is observed that the current expression can be rewritten as the sum of its harmonic components [47]

$$
I_{(n)}(t) = V_0 \sum_{n=0} \left[G_{(n)} \cos(n\omega t) - B_{(n)} \sin(n\omega t) \right]. \quad (3.20)
$$

This decomposition provides a clearer understanding of the contributions from each frequency component. Comparing the two current expressions, (3.19) and (3.20), the terms inside the braces are identified and grouped into the n-modes of conductance, $G_{(n)}$, and susceptance, $B_{(n)}$. This work considers terms up to the second order, i.e., $n = 1, 2$. For the first order, they are given by

$$
G_{(1)} = \frac{A}{V_0} \left[\frac{\sigma_1^{(p)} \left(\omega\tau^{(p)}\right)^2}{1+\left(\omega\tau^{(p)}\right)^2} - \frac{\sigma_1^{(lk)} \left(\omega\tau^{(lk)}\right)^2}{1+\left(\omega\tau^{(lk)}\right)^2} \right] + G_0, \quad (3.21)
$$

$$
B_{(1)} = \frac{A}{V_0} \left[\frac{\sigma_1^{(p)} \omega\tau^{(p)}}{1+(\omega\tau^{(p)})^2} - \frac{\sigma_1^{(lk)} \omega\tau^{(lk)}}{1+(\omega\tau^{(lk)})^2} \right] + \omega C. \quad (3.22)
$$

For the second order, they are:

$$
G_{(2)} = \frac{2A}{V_0} \left[\frac{\sigma_2^{(p)} (\omega\tau^{(p)})^2}{1+(\omega\tau^{(p)})^2} - \frac{\sigma_2^{(lk)} (\omega\tau^{(lk)})^2}{1+(\omega\tau^{(lk)})^2} \right], \quad (3.23)
$$

$$
B_{(2)} = \frac{A}{V_0} \left[\frac{\sigma_2^{(p)} \omega\tau^{(p)}}{1+(\omega\tau^{(p)})^2} - \frac{\sigma_2^{(lk)} \omega\tau^{(lk)}}{1+(\omega\tau^{(lk)})^2} \right]. \quad (3.24)
$$

The term $G_{(n)}$ represents the conductance, which quantifies the material's ability to conduct electric current and is the inverse of resistance, R [69]. Conversely, the term $B_{(n)}$ represents the susceptance, which corresponds to the imaginary part of the admittance, $Y_{(n)}$, a measure of how easily a circuit or component allows the flow of current when subjected to an applied voltage [70]. These quantities are related as

$$
Y_{(n)}(\omega) = G_{(n)}(\omega) + iB_{(n)}(\omega), \quad (3.25)
$$

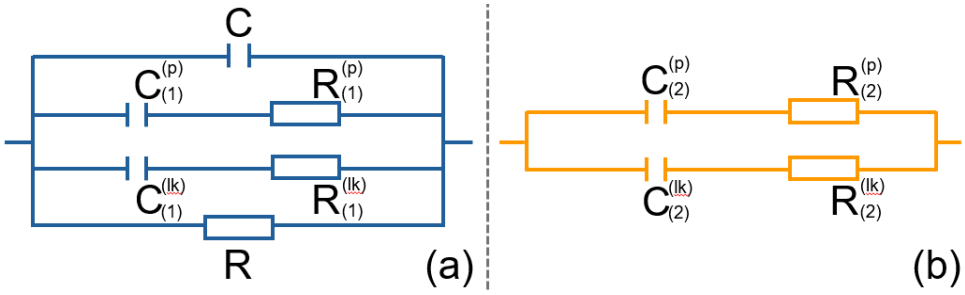

Figure 6 – Apparent circuit representations illustrating the (a) first and (b) second modes of impedance.

where i is the imaginary unit. By explicitly defining the n-modes of admittance (3.25), along with (3.21), (3.22), (3.23), and (3.24), we obtain

$$Y_{(1)}(\omega) = \frac{A}{V_0}\left[\frac{\sigma_1^{(p)}\left(\omega\tau^{(p)}\right)^2}{1+\left(\omega\tau^{(p)}\right)^2} - \frac{\sigma_1^{(lk)}\left(\omega\tau^{(lk)}\right)^2}{1+\left(\omega\tau^{(lk)}\right)^2}\right] + G_0 + i\left\{\frac{A}{V_0}\left[\frac{\sigma_1^{(p)}\omega\tau^{(p)}}{1+(\omega\tau^{(p)})^2} - \frac{\sigma_1^{(lk)}\omega\tau^{(lk)}}{1+(\omega\tau^{(lk)})^2}\right] + \omega C\right\}, \quad (3.26)$$

$$Y_{(2)}(\omega) = \frac{2A}{V_0}\left[\frac{\sigma_2^{(p)}(\omega\tau^{(p)})^2}{1+(\omega\tau^{(p)})^2} - \frac{\sigma_2^{(lk)}(\omega\tau^{(lk)})^2}{1+(\omega\tau^{(lk)})^2}\right] + \left\{\frac{A}{V_0}\left[\frac{\sigma_2^{(p)}\omega\tau^{(p)}}{1+i(\omega\tau^{(p)})^2} - \frac{\sigma_2^{(lk)}\omega\tau^{(lk)}}{1+(\omega\tau^{(lk)})^2}\right]\right\}. \quad (3.27)$$

Since $\tau' = R'C'$, the admittance expression (3.26) leads to the following apparent resistances R' and capacitances C' for $n = 1$

$$R \equiv \frac{1}{G_0}, \quad (3.28)$$

$$R_{(1)}^{(p)} = \frac{V_0}{A\sigma_{(1)}^{(p)}}, \quad (3.29)$$

$$R_{(1)}^{(lk)} = -\frac{V_0}{A\sigma_{(1)}^{(lk)}}, \quad (3.30)$$

$$C_{(1)}^{(p)} = \frac{\tau^{(p)}}{R_{(1)}^{(p)}}, \quad (3.31)$$

$$C_{(1)}^{(lk)} = -\frac{\tau^{(lk)}}{R_{(1)}^{(lk)}}. \quad (3.32)$$

Notably, the resistance associated with leakage, $R_{(1)}^{(lk)}$, in Equation (3.30), carries a negative sign, indicating that it opposes its contribution to the total resistance R to charge flux. Similarly, the capacitance related to leakage, $C_{(1)}^{(lk)}$, in Equation (3.32), also exhibits a negative sign, which, depending on the chosen parameters, can give rise to negative capacitance effects—an occurrence that has been experimentally observed [71–75]. Figure 6(a) represents the apparent circuit formed by the expressions from (3.28) to (3.32).

Applying the same procedure for $n = 2$, the admittance in Equation (3.27) yields the following expressions for the resistances R' and capacitances C'

$$R_{(2)}^{(p)} = \frac{2V_0}{A\sigma_{(2)}^{(p)}}, \tag{3.33}$$

$$R_{(2)}^{(lk)} = -\frac{2V_0}{A\sigma_{(2)}^{(lk)}}, \tag{3.34}$$

$$C_{(2)}^{(p)} = \frac{2\tau^{(p)}}{R_{(2)}^{(p)}}, \tag{3.35}$$

$$C_{(2)}^{(lk)} = -\frac{2\tau^{(lk)}}{R_{(2)}^{(lk)}}. \tag{3.36}$$

The signs in the expressions above do not fully determine their behavior, as the asymmetry parameter α present in $\sigma_2^{(\gamma)}$ (Equation (3.5)) introduces ambiguity. The apparent circuit formed by the second-mode expressions, from (3.33) to (3.36), is presented in Figure 6(b).

In this work, we adopt the term *apparent circuit* instead of *equivalent circuit* to emphasize the phenomenological nature of the impedance representation derived from the model. Traditional equivalent circuit models are constructed by directly associating physical components—such as resistors, capacitors, and inductors—with well-defined microscopic mechanisms in the material. However, in the present case, the circuit elements emerge from a multimodal impedance analysis that captures complex interactions between charge transport, polarization dynamics, and leakage effects. These elements do not necessarily correspond to discrete physical components but rather serve as effective representations of the material's response under an applied field. The *apparent circuit* thus provides a practical means to describe the system's behavior in the frequency domain, enabling meaningful comparisons with experimental impedance spectroscopy data, while acknowledging that the underlying transport processes may not adhere strictly to lumped-element circuit analogies. This distinction is particularly relevant when dealing with systems exhibiting nonlinearities, memory effects, or nonequilibrium charge dynamics, where conventional equivalent circuits may fail to fully capture the material's response.

Similarly, another fundamental electrical quantity, impedance $Z(\omega)$, can also be expressed in terms of conductance $G_{(n)}$ and susceptance $B_{(n)}$, since impedance is the inverse of admittance (3.25), i.e., $Y = 1/Z$. Consequently, the impedance modes can be described as

$$Z_{(n)}(\omega) = \frac{G_{(n)}(\omega)}{[G_{(n)}(\omega)]^2 + [B_{(n)}(\omega)]^2} - i\frac{B_{(n)}(\omega)}{[G_{(n)}(\omega)]^2 + [B_{(n)}(\omega)]^2}. \tag{3.37}$$

Equation (3.37) reveals that impedance $Z(\omega)$ consists of both a real and an imaginary component. The real part corresponds to the system's resistivity, representing

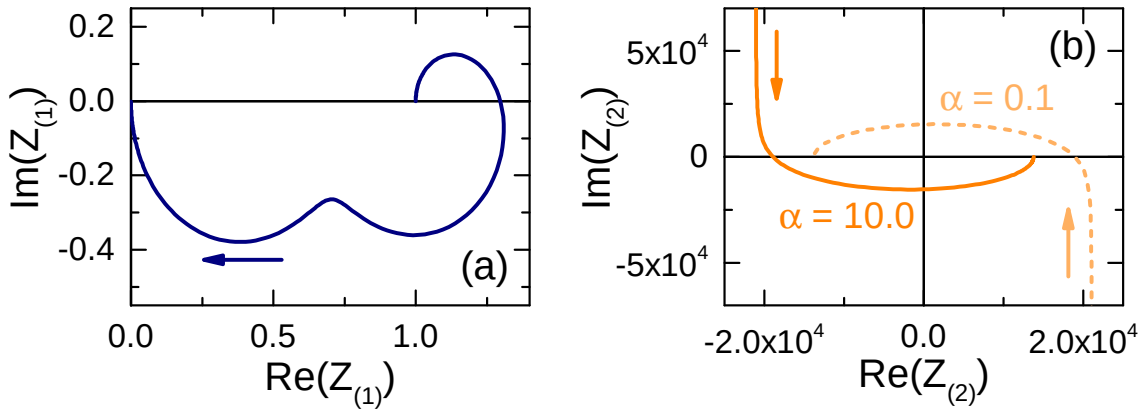

Figure 7 – (a) First-order, and (b) Second-order of Nyquist plot. The parameters are detailed in Table 1 of the Appendix A.

opposition to current flow, while the imaginary part is linked to its reactance, which describes the system's response to variations in the electric field [65].

The first impedance mode, corresponding to $n = 1$, can be explicitly formulated by incorporating conductance (3.21), susceptance (3.22), as well as $\lambda^{(\gamma)}$ (Equation (2.30)) and $\sigma_1^{(\gamma)}$ (Equation (3.4)). These terms account for both internal polarization (p) and leakage (lk)

$$Z_{(1)} = \left\{ \frac{4\pi m^*}{(2\pi\hbar)^3} e^2 \eta A k_B T_{eff} \frac{(\alpha^2+1)}{(\alpha+1)^2} \left[\frac{\omega\tau^{(p)} \exp\left[-E^{(p)}/(k_B T_{eff})\right]}{1+(\omega\tau^{(p)})} (\omega\tau^{(p)} + i) \right.\right. \\ \left.\left. - \frac{\omega\tau^{(lk)} \exp\left[-E^{(lk)}/(k_B T_{eff})\right]}{1+(\omega\tau^{(lk)})} (\omega\tau^{(lk)} + i) \right] + G_0 + i\omega C \right\}^{-1} \tag{3.38}$$

A similar approach can be applied to the second impedance mode, $n = 2$, using conductance (3.23), susceptance (3.24), and $\sigma_2^{(\gamma)}$ as defined in (3.5)

$$Z_{(2)} = \left\{ \frac{2\pi m^*}{(2\pi\hbar)^3} e^3 \eta^2 A V_0 \frac{(\alpha^3-1)}{(\alpha+1)^3} \left[\frac{\omega\tau^{(p)} \exp\left[-E^{(p)}/(k_B T_{eff})\right]}{1+(\omega\tau^{(p)})} (2\omega\tau^{(p)} + i) \right.\right. \\ \left.\left. - \frac{\omega\tau^{(lk)} \exp\left[-E^{(lk)}/(k_B T_{eff})\right]}{1+(\omega\tau^{(lk)})} (2\omega\tau^{(lk)} + i) \right] \right\}^{-1} \tag{3.39}$$

The multimodal impedance expression (3.38) for $n = 1$ produces the Nyquist plot shown in Figure 7(a), where it is observed that the imaginary contribution assumes positive values at low frequencies ω, a phenomenon associated with negative capacitance effects [75]. Figure 7(b) illustrates the impedance for $n = 2$, where the second mode exists only in asymmetric systems, i.e., $\alpha \neq 1$. Furthermore, as the frequency ω increases, the impedance sign changes: initially, the real part is negative and the imaginary part is positive, but at higher frequencies, the opposite occurs. This behavior, absent in the $n = 1$ mode, also exhibits a mirroring effect when symmetry is modified to proportional values in the second

mode, with $\alpha = 10^{1}$ and $\alpha = 10^{-1}$, demonstrating that the contributions of the second mode are essential to understanding the true impedance values of a system.

3.3 Dielectric spectroscopy

In this study, a connection is also established between impedance spectroscopy and dielectric spectroscopy. This approach enables the measurement of dielectric permittivity, which characterizes the material's ability to store electrical energy, and dielectric loss, which quantifies the energy dissipated as heat [66]. Both quantities are evaluated as functions of frequency. In the case of a polarization disturbance, a multimode analysis can be conducted, where $\delta P = \varepsilon_0 \sum_{n=1} \chi_{(n)} E^n$. Thus, he total polarization can be expressed as

$$P = \varepsilon_0 \chi_\infty E + \varepsilon_0 \sum_{n=1} \chi_{(n)} E^n. \tag{3.40}$$

The first term in Equation (3.40) corresponds to the instantaneous polarization P_∞, previously described in Equation (2.32). To analyze the system's frequency response, a modified complex potential function is introduced, which is a rather standard procedure

$$V(t) = V_0 e^{i\omega t}. \tag{3.41}$$

By applying this potential (3.41) to the electric field (2.33), the polarization (3.40) can be rewritten as a multimode expansion

$$P(t) = \varepsilon_0 \chi_\infty \frac{V_0}{d} e^{i\omega t} + \varepsilon_0 \sum_{n=1} \chi_{(n)} \left(\frac{V_0}{d}\right)^n e^{in\omega t}. \tag{3.42}$$

Following the same procedure as before, by taking the time derivative of the polarization and electric field, the total displacement current (2.36) is obtained with the terms appropriately grouped

$$j_D = \varepsilon_0 \left(1 + \chi_\infty\right) i\omega \frac{V_0}{d} e^{i\omega t} + \varepsilon_0 \sum_{n=1} \chi_{(n)} in\omega \left(\frac{V_0}{d}\right)^n e^{in\omega t}. \tag{3.43}$$

Considering the material's permittivity ε_∞, given by $\varepsilon_\infty = \varepsilon_0(1+\chi_\infty)$, the total current can be obtained by substituting the new displacement current into Equation (2.40). Expanding the first term of the summation and assuming $G_0 \gg \Gamma \delta n$, we obtain

$$I = \left(\varepsilon_\infty + \varepsilon_0 \chi_{(1)} - i\frac{G_0 d}{\omega A}\right) i\omega A \frac{V_0}{d} e^{i\omega t} + \varepsilon_0 \sum_{n=2} \chi_{(n)} in\omega A \left(\frac{V_0}{d}\right)^n e^{in\omega t}. \tag{3.44}$$

In turn, in order to express the total current in a more compact and insightful manner, it is rewritten as a summation of its harmonic components

$$I_{(n)} = A \sum_{n=1} i\varepsilon_{(n)} n\omega \left(\frac{V_0}{d}\right)^n e^{in\omega t}, \tag{3.45}$$

where the permittivity per mode, $\varepsilon_{(n)}$, arises from the multimode perspective and is defined as

$$\varepsilon_{(n)} = \varepsilon_0 \chi_{(n)} + \delta_{n,1} \left[\varepsilon_0 (1 + \chi_\infty) - i \frac{G_0}{\omega} \frac{d}{A} \right] \tag{3.46}$$

The term $\delta_{n,1}$ is a Kronecker delta, which takes the value $\delta_{n,1} = 1$ for $n = 1$ and $\delta_{n,1} = 0$ for $n \neq 1$. However, an equivalent expression for the current, similar to Equation (3.20), can be formulated in terms of the new potential (3.41) in the complex plane

$$I_{(n)} = V_0 \sum_{n=1} \left[G_{(n)} + i B_{(n)} \right] e^{in\omega t}. \tag{3.47}$$

Equating expressions (3.45) and (3.47) reveals an interesting relationship

$$A \sum_{n=1} i \varepsilon_{(n)} n\omega \left(\frac{V_0}{d} \right)^n e^{in\omega t} = V_0 \sum_{n=1} \left[G_{(n)} + i B_{(n)} \right] e^{in\omega t}. \tag{3.48}$$

By isolating the permittivity term in Equation (3.48), a new expression is obtained that determines the permittivity modes based on conductance $G_{(n)}$ and susceptance $B_{(n)}$

$$\varepsilon_{(n)} = \frac{[B_{(n)} - i G_{(n)}]}{n\omega} \frac{d^n}{A V_0^{n-1}} \tag{3.49}$$

For $n = 1$, the first-mode permittivity is obtained by substituting $\lambda^{(\gamma)}$ from Equation (2.30) into Equation (3.4), and then incorporating the corresponding $\sigma^{(\gamma)}$ into conductance (3.21) and susceptance (3.22), leading to

$$\varepsilon_{(1)} = \frac{4\pi m^*}{(2\pi\hbar)^3} e^2 \eta d k_B T_{eff} \frac{(\alpha^2 + 1)}{(\alpha + 1)^2} \left\{ \frac{\tau^{(p)} \exp[-E^{(p)}/(k_B T_{eff})]}{1 + (\omega\tau^{(p)})^2} (1 - i\omega\tau^{(p)}) \right.$$
$$\left. - \frac{\tau^{(lk)} \exp[-E^{(lk)}/(k_B T_{eff})]}{1 + (\omega\tau^{(lk)})^2} (1 - i\omega\tau^{(lk)}) \right\} + \frac{d}{\omega A} (\omega C - i G_0) \tag{3.50}$$

Using the same parameters as in Figure 7(a), the real component of the first-mode permittivity, $\mathrm{Re}(\varepsilon_{(1)})$, is plotted as a function of frequency ω in Figure 8(a). The proportionality $\mathrm{Re}(\varepsilon_{(1)}) \propto B_{(1)}/\omega$ reveals a step-like behavior in the logarithmic scale, which increases when internal polarization dominates over leakage and decreases when leakage prevails. Meanwhile, the imaginary component, shown in Figure 7(b), diverges for small ω, since $\mathrm{Im}(\varepsilon_{(1)}) \propto -G_0/\omega$.

For $n = 2$, the second-mode permittivity is determined using conductance (3.23) and susceptance (3.24)

$$\varepsilon_{(2)} = \frac{2\pi m^*}{(2\pi\hbar)^3} e^3 \eta^2 d^2 \frac{(\alpha^3 - 1)}{(\alpha + 1)^3} \left\{ \frac{\tau^{(p)} \exp[-E^{(p)}/(k_B T_{eff})]}{1 + (\omega\tau^{(p)})^2} \left(\frac{1}{2} - i\omega\tau^{(p)} \right) \right.$$
$$\left. - \frac{\tau^{(lk)} \exp[-E^{(lk)}/(k_B T_{eff})]}{1 + (\omega\tau^{(lk)})^2} \left(\frac{1}{2} - i\omega\tau^{(lk)} \right) \right\} \tag{3.51}$$

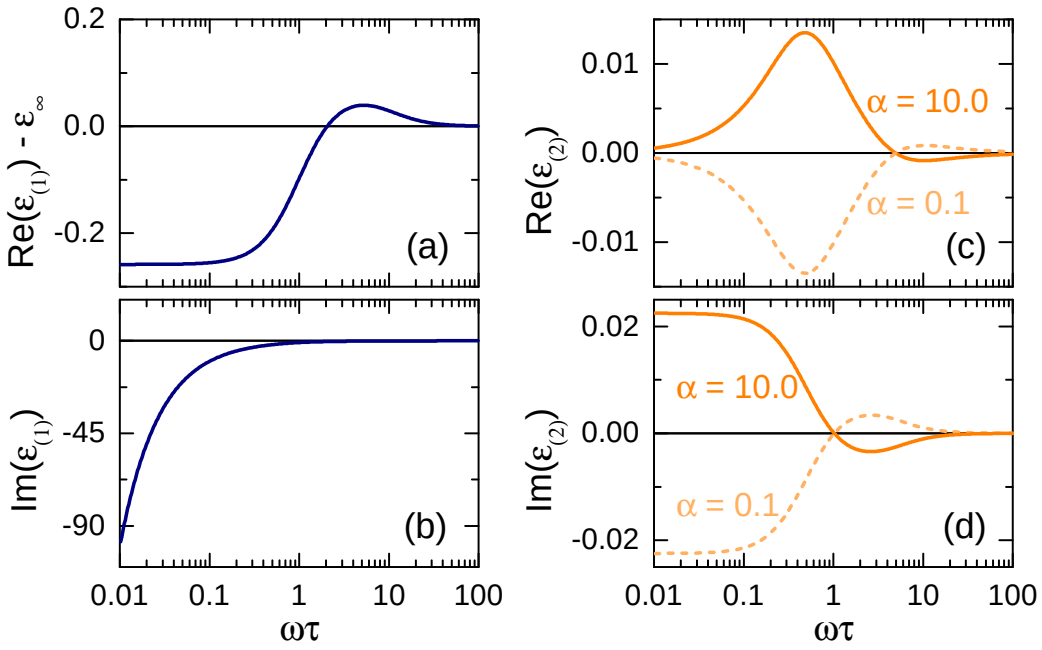

Figure 8 – First-order results: (a) real part, and (b) imaginary part of the dielectric permittivity. Second-order results: (c) real part, and (d) imaginary part of the dielectric permittivity. The parameters are detailed in Table 1 of the Appendix A.

In this case, the real part of the permittivity, $\mathrm{Re}(\varepsilon_{(2)})$, also exhibits step-like variations, as shown in Figure 8(a). This behavior arises for the same reason as in the first mode, although the amplitude of the effect is smaller, despite using the same parameter set. Additionally, a direct proportional relationship between the real part of the permittivity and the second mode of the susceptance is observed, following $\mathrm{Re}(\varepsilon_{(2)}) \propto B_{(2)}/\omega$.

The imaginary component of the second-mode permittivity, $\mathrm{Im}(\varepsilon_{(2)})$, behaves differently, collapsing at both high and low frequencies ω, indicating a reduced contribution to the overall dielectric response in these regimes. This collapse suggests that the second mode plays a significant role only within an intermediate frequency range. Furthermore, the mirroring effect observed in the second mode of the Nyquist plot for impedance (Figure 7(b)) is also evident in the permittivity plots shown in Figures 8(c) and (d). This symmetry highlights the impact of charge transport asymmetry on the dielectric response and suggests that reversing the system's asymmetry parameter α leads to a corresponding inversion in the permittivity spectrum.

Another crucial aspect of the permittivity expressions per mode is their dependence on the system's effective temperature, T_{eff}. The real part of the first mode of permittivity, given by Equation (3.50), includes an explicit temperature factor within the exponential term, which is further externally multiplied by additional prefactors. This temperature dependence significantly influences the dielectric response. Figure 9(a) illustrates this behavior for various voltage sweep periods T. At short periods (high frequencies ω), the system exhibits a monotonic decrease in permittivity, consistent with conventional

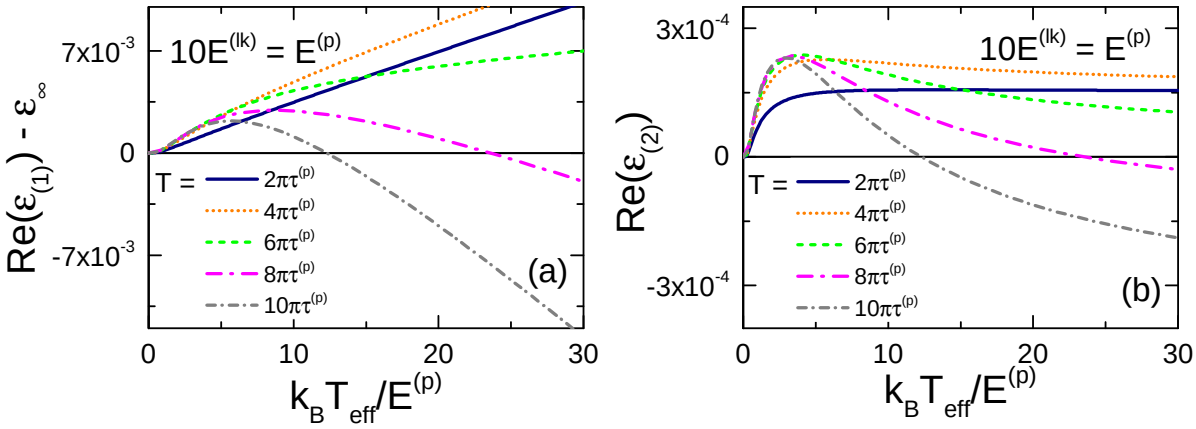

Figure 9 – Real part of the (a) first mode and (b) second mode of the dielectric permittivity $\varepsilon_{(n)}$ as a function of temperature T_{eff}, with varying periods T. The leakage energy barrier $E^{(lk)}$ was set to 10 times the internal energy barrier $E^{(p)}$. Additional parameters are listed in Table 1 of Appendix A.

dielectric materials. However, as the frequency decreases, this monotonic trend disappears, giving way to a frequency-dependent peak, a hallmark of relaxor ferroelectrics [76, 77]. In such systems, the dielectric permittivity exhibits strong dispersion with frequency, reflecting underlying polarization dynamics and disorder effects [21].

For the second mode, given by Equation (3.51), the temperature dependence appears only within the exponential terms, leading to a distinct response compared to the first mode. As shown in Figure 9(b), the second-mode permittivity does not exhibit a monotonic trend for the same parameter set used previously. However, for longer voltage sweep periods (lower frequencies), the behavior gradually aligns with the first mode, indicating a similar frequency-dependent relaxation effect [2]. This suggests that higher-order polarization contributions become relevant only in specific frequency regimes, reinforcing the importance of multimode analysis in capturing the full dielectric response of the system.

4 Applications for Mememitter Functionalities

In a recent study, the concept of *Mem-emitters* was introduced, referring to devices engineered to regulate and modulate the light emission properties of semiconductor materials. These components are particularly significant for optoelectronic computing applications [78], as they leverage memory functionalities inspired by the resistive switching behavior observed in memristors [32]. The fundamental idea behind the definition of a mem-emitter is straightforward and originates from the memristor concept introduced in Ref. [79].

To describe the mem-emitter response, we consider that the intensity of emitted light, Q, is proportional to the population N of the initial state and the optical transition rate $1/\tau$, given by

$$Q = \frac{N}{\tau}. \tag{4.1}$$

The optical transition rate can be expressed in terms of the optical transition matrix elements, $K_{f,i}$, which describe the transition probability between the initial (i) and final (f) states, and an energy conservation factor, $D(\Delta E_{f,i} - \hbar\omega)$, which ensures that emission occurs at the correct energy

$$\frac{1}{\tau} = K_{f,i} \cdot D(\Delta E_{f,i} - \hbar\omega). \tag{4.2}$$

Then, for a system to exhibit mem-emitter behavior, the key emission parameters—namely, the transition probability $K_{f,i}(\mathbf{F}, \mathbf{x}, t)$, the transition energy $\Delta E_{f,i}(\mathbf{F}, \mathbf{x}, t)$, and the initial-state population $N(\mathbf{F}, \mathbf{x}, t)$—must dynamically depend on a set of internal state variables, $\mathbf{x}$. The evolution of these internal variables follows a time-dependent equation

$$\frac{d\mathbf{x}}{dt} = f(\mathbf{F}, \mathbf{x}, t), \tag{4.3}$$

where $\mathbf{F}$ represents external control fields such as electric or optical excitation.

This time-dependent relationship implies that the light emission intensity, Q, and its spectral position are not solely determined by the instantaneous external fields $\mathbf{F}$ but also by the internal state of the system, represented by $\mathbf{x}$. As a result, the emission exhibits an adaptive, history-dependent behavior, analogous to memristive responses in electronic systems. This property makes mememitters promising candidates for applications in reconfigurable optoelectronic circuits and neuromorphic photonic computing.

A promising architecture for mem-emitter capacitors involves the use of two distinct materials as the dielectric filling. Figure 10(a) illustrates such a configuration, where the left side of the capacitor is composed of two-dimensional functional heterostructures of transition metal dichalcogenide (TMD) monolayers, characterized by their unique memory

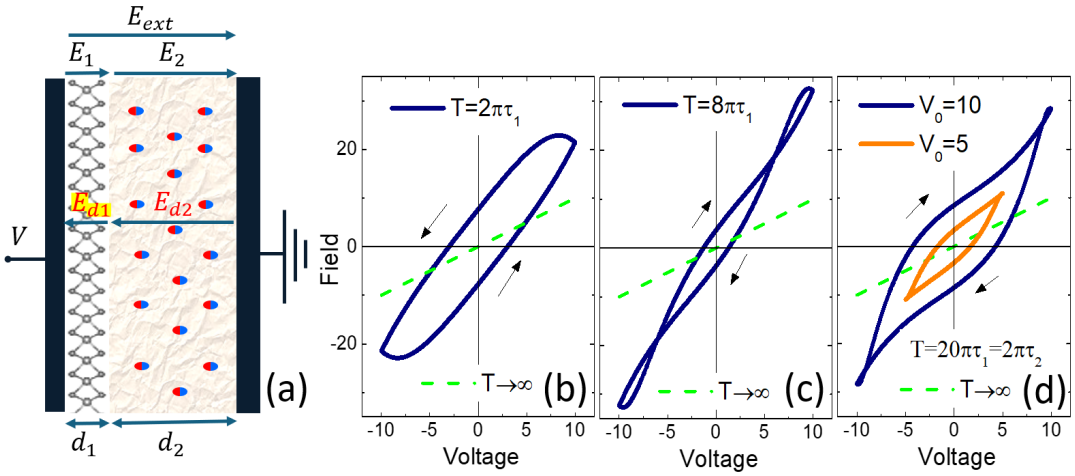

Figure 10 – (a) Schematic representation of a capacitor composed of two dielectric materials: a two-dimensional transition metal dichalcogenide with thickness d_1 and a dielectric substrate with thickness d_2. Stable cycles of the electric field for varying period: (b) $T = 2\pi\tau_1$, (c) $T = 8\pi\tau_1$, and (d) $T = 20\pi\tau_1 = 2\pi\tau_2$, also presenting an electric field for a voltage with half the amplitude. Dashed lines indicate the collapse of the hysteresis for very long periods and the arrows point to the direction of the voltage sweep.

properties, which are crucial for enabling mem-emitter functionalities [80,81]. The thickness of this TMD region is denoted as d_1. On the right side, a dielectric substrate with thickness d_2 is present, serving both as structural support for the TMD monolayer and as an active component influencing the overall electric field distribution and polarization properties of the system.

When an external electric field E_{ext} is applied across the capacitor, it distributes between the two materials such that the TMD layer experiences a field E_1 and the dielectric substrate experiences a field E_2. Consequently, the total potential difference V across the system is given by

$$V = E_1 d_1 + E_2 d_2. \tag{4.4}$$

However, the application of an external electric field induces charge movement within the materials as emulated in the previous chapters, leading to polarization. This polarization, in turn, generates an internal field E_{d_j} that opposes the applied field. The net field within each material is thus given by

$$E_j = E_{\text{ext}} - E_{d_j} = E_{\text{ext}} - \frac{P_j}{\varepsilon_0}, \tag{4.5}$$

where P_j represents the polarization in material j, and ε_0 is the vacuum permittivity. According to the model, the polarization in each region consists of two components: an instantaneous response P_∞ and a fluctuating component δP_j around an equilibrium state

$$P_j = P_\infty + \delta P_j = \varepsilon_0 \chi_j E_j + \delta P_j \tag{4.6}$$

Here, χ_j represents the dielectric susceptibility of material j, which determines its response to the applied electric field E_j. By substituting Equation (4.6) into Equation (4.5), we

obtain a relationship linking the internal fields in each region to the external field

$$E_j = \frac{E_{\text{ext}}}{1+\chi_j}. \tag{4.7}$$

This result indicates that the internal field in each material is inversely proportional to its dielectric susceptibility. As susceptibility increases, the internal field decreases, and vice versa. Similarly, substituting Equation (4.7) into Equation (4.6) allows us to express the polarization in terms of the external electric field

$$P_j = \frac{\varepsilon_0 \chi_j E_{\text{ext}}}{1+\chi_j} + \delta P_j. \tag{4.8}$$

To express the total potential V in terms of the external field E_{ext}, we substitute Equation (4.8) into Equation (4.4), yielding

$$V = \frac{E_{\text{ext}} d_1}{1+\chi_1} + \left(E_{\text{ext}} - \frac{\chi_2}{1+\chi_2} E_{\text{ext}} - \frac{\delta P_2}{\varepsilon_0} \right) d_2. \tag{4.9}$$

In this expression, χ_1 represents the dielectric susceptibility of the TMD monolayer, while χ_2 is that of the dielectric substrate. The term δP_2 accounts for fluctuations in the polarization of the dielectric substrate.

Rearranging this equation, we isolate the external field E_{ext} in terms of the applied potential and polarization fluctuations

$$E_{\text{ext}} = \left(V + \frac{\delta P_2 d_2}{\varepsilon_0} \right) \frac{(1+\chi_1)(1+\chi_2)}{d_1(1+\chi_2) + d_2(1+\chi_1)}. \tag{4.10}$$

By substituting Equation (4.10) into Equation (4.7), we obtain an expression for the field within the TMD monolayer

$$E_1 = \left(V + \frac{\delta P_2 d_2}{\varepsilon_0} \right) \frac{(1+\chi_2)}{d_1(1+\chi_2) + d_2(1+\chi_1)}. \tag{4.11}$$

For systems where the TMD monolayer thickness is significantly smaller than that of the dielectric substrate ($d_1 \ll d_2$), this simplifies to

$$E_1 = \left(\frac{V}{d_2} + \frac{\delta P_2}{\varepsilon_0} \right) \frac{(1+\chi_2)}{(1+\chi_1)} \tag{4.12}$$

Panels 10(b), (c), and (d) present the electric field evolution in the TMD layer under a triangular voltage drive. The resulting field curves exhibit patterns analogous to those observed in Figure 4(h-i), where an increase in the voltage sweep period leads to a reversal in polarization direction.

Since the optical transition rate in the TMD layer and the emitted photon energy are both proportional to the local electric field, i.e., $K_{f,i} \propto E_1$ and $\Delta E_{f,i} \propto E_1$, it follows that these optical properties will exhibit dynamic behavior corresponding to the loops

shown in Figures 10(b), (c), and (d). Thus, according to Equation (4.3), the key internal state variable governing the Mem-emitter response is the polarization fluctuation in the dielectric substrate, which evolves according to the differential equation (2.34).

The distinctive optical signatures that arise from these polarization dynamics can serve as valuable tools for device characterization. For instance, by analyzing these unique emission patterns, crucial material properties and system behaviors can be inferred, aiding in the optimization of device performance. Beyond characterization, these peculiar optical responses hold potential for advanced applications in information transmission and processing. Furthermore, the ability to encode information in dynamic optical signals suggests new possibilities for data encoding schemes in next-generation communication systems, leveraging the memory-dependent properties of Mem-emitters for enhanced signal processing capabilities.

5 Conclusions

The model proposed in this work provides a comprehensive framework for describing transfer functions and the evolution of fluctuations in internal polarization and charge leakage around an equilibrium point, up to the relaxation time, as formulated in equation (2.34). By capturing the interplay between these mechanisms, the model characterizes the dielectric responses of materials that are not necessarily polar or ferroelectric. This generalization allows for a more robust understanding of dielectric behavior, offering a unified approach to analyzing polarization dynamics. Furthermore, it successfully replicates experimentally observed hysteresis behaviors, bridging theoretical predictions with experimental findings. Notably, it accounts for polarization and current reversal, as well as ferroelectric-like hysteresis in leaky dielectrics.

Beyond its fundamental insights into polarization dynamics and charge transport, the model enhances the accurate characterization of materials used in capacitors, transistors, and memory devices.

The first-order harmonics introduced in the model for impedance spectroscopy further validate its ability to accurately describe Nyquist curves, with theoretical predictions closely matching experimental observations. In particular, the model successfully captures positive impedance curves at low frequencies, in agreement with previously reported experimental data [71–75]. The analysis of the second harmonic mode reveals additional critical effects, emphasizing its significance for systems primarily governed by displacement currents.

Furthermore, the description of dielectric permittivity within this framework introduces a novel methodology for determining its values based on both conductivity and susceptibility modes, effectively integrating two traditionally distinct approaches for dielectric characterization. The inclusion of temperature-dependent permittivity is particularly relevant for modeling ferroelectric relaxors, where temperature variations significantly influence the system's behavior [2, 76, 77].

In dynamic nonlinear systems, the application of a sinusoidal signal, as commonly employed in impedance and dielectric spectroscopy, can induce responses not only at the fundamental frequency but also at higher harmonics due to system nonlinearities. Analyzing only the fundamental mode neglects critical information embedded within these higher harmonics, which can be essential for uncovering the true nature of the system's nonlinearity.

For instance, the amplitude and phase of these higher harmonics provide insight into the strength and type of nonlinearities present, such as harmonic generation, sat-

uration effects, or memory-related behaviors. A multimode analysis that accounts for these higher-order modes offers a more comprehensive understanding of system dynamics, uncovering hidden information that would otherwise be overlooked by focusing solely on the fundamental response.

Future Research and Applications

This study demonstrates the robustness of the proposed model in capturing a wide range of dielectric behaviors by analyzing dipole perturbations, integrating both internal polarization effects and charge leakage dynamics. Moving forward, future research could focus on the response of specific materials under varying external conditions, including:

- **Temperature variations**: Investigating temperature-dependent polarization dynamics and their impact on dielectric relaxation.
- **Illumination effects**: Exploring light-matter interactions and their role in charge trapping and transport mechanisms.
- **Electromagnetic fields**: Extending the model to analyze the influence of external electromagnetic fields on dielectric and memristive properties.

Additionally, this work explores the potential of leveraging dielectric materials for **Mem-emitter functionalities**. Their tunable electronic properties and strong light-matter interactions make them ideal candidates for advanced optoelectronic applications. The insights presented in this dissertation may contribute to the development of novel memory and computing technologies that integrate optoelectronic and memristive properties for improved efficiency and functionality.

The findings of this study pave the way for an in-depth analysis of non-equilibrium effects in dielectrics and low-conductivity materials. Future work will involve the integration of both drift and displacement currents in transport property analyses, potentially unveiling new phenomena such as resonant behaviors in individual devices. Furthermore, incorporating illumination effects will introduce additional complexity, necessitating refinements in the theoretical model to account for interactions between charge transport and optical excitations.

Ultimately, we hope that the methodologies and insights presented in this dissertation may contribute to the broader understanding of nonequilibrium processes in dielectric materials, offering a foundation for future advancements in energy storage, computing, and optoelectronic technologies.

Bibliography

[1] Hari Prashanth Palani Velayuda Shanmugasundram, Elammaran Jayamani, and Kok Heng Soon. A comprehensive review on dielectric composites: Classification of dielectric composites. *Renewable and Sustainable Energy Reviews*, 157:112075, 2022. Mentioned on the page 14.

[2] Xiaojun Wu, Lanji Wen, Chao Wu, Xiang Lv, Jie Yin, and Jiagang Wu. Insight into the large electro-strain in bismuth sodium titanate-based relaxor ferroelectrics: From fundamentals to regulation methods. *Journal of Materials Science & Technology*, 150:27–48, 2023. Mentioned 3 times in the pages 14, 44, and 49.

[3] Liu Hongbo. Dielectrics under electric field. *Electric Field*, 2018. Mentioned on the page 14.

[4] Christian Wiraja and Yanli Zhao. Toward miniaturizing microelectronics using covalent organic framework dielectric. *Matter*, 4(6):1760–1762, 2021. Mentioned on the page 14.

[5] Rajeev Gupta, Adesh Kumar, A Biswas, Rajesh Singh, Anita Gehlot, Shaik Vaseem Akram, and Ajay Singh Verma. Advances in micro and nano-engineered materials for high-value capacitors for miniaturized electronics. *Journal of Energy Storage*, 55:105591, 2022. Mentioned on the page 14.

[6] D. Walsh L. Solymar and R. R. A. Syms. *Electrical Properties of Materials*. Oxford, United Kingdom, 2019. Mentioned on the page 14.

[7] Ratanak Lay, Gerrit Sjoerd Deijs, and Jenny Malmström. The intrinsic piezoelectric properties of materials–a review with a focus on biological materials. *RSC advances*, 11(49):30657–30673, 2021. Mentioned on the page 14.

[8] Jiashun Si, Xuefeng Xiao, Yan Zhang, Yan Huang, Shuaijie Liang, Qingyan Xu, Huan Zhang, Lingling Ma, Cui Yang, and Xuefeng Zhang. Pyroelectric properties and applications of lithium tantalate crystals. *Crystals*, 14(7):579, 2024. Mentioned on the page 14.

[9] A Ray, M Nayak, H Joardar, S Sahoo, T Badapanda, P Jena, SK Mishra, R Mittal, and Satya N Tripathy. Investigation of dynamic scaling behavior, electrocaloric performance, and pyroelectric energy storage of ba0. 85ca0. 15ti0. 9zr0. 1o3 ceramic. *Chemical Physics Impact*, 8:100555, 2024. Mentioned on the page 14.

[10] Mariya Aleks, Chaitali Jagtap, Vishal Kadam, Georgi Kolev, Krasimir Denishev, Habib Pathan, et al. An overview of microelectronic infrared pyroelectric detector. *Engineered Science*, 16:82–89, 2021. Mentioned on the page 14.

[11] Jiaxing Guo, Wenwen Chen, Haisheng Chen, Yanan Zhao, Feng Dong, Weiwei Liu, and Yang Zhang. Recent progress in optical control of ferroelectric polarization. *Advanced Optical Materials*, 9(23):2002146, 2021. Mentioned on the page 15.

[12] Boyuan Cui, Zhen Fan, Wenjie Li, Yihong Chen, Shuai Dong, Zhengwei Tan, Shengliang Cheng, Bobo Tian, Ruiqiang Tao, Guo Tian, et al. Ferroelectric photosensor network: an advanced hardware solution to real-time machine vision. *Nature Communications*, 13(1):1707, 2022. Mentioned on the page 15.

[13] Yang Liu, Yao Zhou, Hancheng Qin, Tiannan Yang, Xin Chen, Li Li, Zhubing Han, Ke Wang, Bing Zhang, Wenchang Lu, et al. Electro-thermal actuation in percolative ferroelectric polymer nanocomposites. *Nature Materials*, 22(7):873–879, 2023. Mentioned on the page 15.

[14] Havid Aqoma, Sang-Hak Lee, Imil Fadli Imran, Jin-Ha Hwang, Su-Ho Lee, and Sung-Yeon Jang. Alkyl ammonium iodide-based ligand exchange strategy for high-efficiency organic-cation perovskite quantum dot solar cells. *Nature Energy*, 9(3):324–332, 2024. Mentioned on the page 15.

[15] JA Kittl, Karl Opsomer, M Popovici, Nicolas Menou, Ben Kaczer, Xin Peng Wang, Christoph Adelmann, MA Pawlak, Kazuyuki Tomida, Aude Rothschild, et al. High-k dielectrics for future generation memory devices. *Microelectronic engineering*, 86(7-9):1789–1795, 2009. Mentioned on the page 15.

[16] Joseph Casamento, Steven M Baksa, Drew Behrendt, Sebastian Calderon, Devin Goodling, John Hayden, Fan He, Leonard Jacques, Seung Hoon Lee, Walter Smith, et al. Perspectives and progress on wurtzite ferroelectrics: Synthesis, characterization, theory, and device applications. *Applied Physics Letters*, 124(8), 2024. Mentioned on the page 15.

[17] Weitong Ding, Jing Lu, Xiao Tang, Liangzhi Kou, and Lei Liu. Ferroelectric materials and their applications in activation of small molecules. *ACS omega*, 8(7):6164–6174, 2023. Mentioned on the page 15.

[18] Ping Wang, Ding Wang, Shubham Mondal, Mingtao Hu, Jiangnan Liu, and Zetian Mi. Dawn of nitride ferroelectric semiconductors: from materials to devices. *Semiconductor Science and Technology*, 38(4):043002, 2023. Mentioned on the page 15.

[19] Yongbo Yuan, Zhengguo Xiao, Bin Yang, and Jinsong Huang. Arising applications of ferroelectric materials in photovoltaic devices. *Journal of Materials chemistry A*, 2(17):6027–6041, 2014. Mentioned on the page 15.

[20] Kwan-Ho Kim, Ilya Karpov, Roy H Olsson III, and Deep Jariwala. Wurtzite and fluorite ferroelectric materials for electronic memory. *Nature Nanotechnology*, 18(5):422–441, 2023. Mentioned on the page 15.

[21] Chang Won Ahn, Chang-Hyo Hong, Byung-Yul Choi, Hwang-Pill Kim, Hyoung-Su Han, Younghun Hwang, Wook Jo, Ke Wang, Jing-Feng Li, Jae-Shin Lee, et al. A brief review on relaxor ferroelectrics and selected issues in lead-free relaxors. *Journal of the Korean Physical Society*, 68:1481–1494, 2016. Mentioned 2 times in the pages 15 and 44.

[22] AR Jayakrishnan, José Pedro Basto Silva, K Kamakshi, D Dastan, V Annapureddy, M Pereira, and KC Sekhar. Are lead-free relaxor ferroelectric materials the most promising candidates for energy storage capacitors? *Progress in Materials Science*, 132:101046, 2023. Mentioned on the page 15.

[23] Xin Chen, Hancheng Qin, Xiaoshi Qian, Wenyi Zhu, Bo Li, Bing Zhang, Wenchang Lu, Ruipeng Li, Shihai Zhang, Lei Zhu, et al. Relaxor ferroelectric polymer exhibits ultrahigh electromechanical coupling at low electric field. *Science*, 375(6587):1418–1422, 2022. Mentioned on the page 15.

[24] Peiyao Zhao, Hongxian Wang, Longwen Wu, Lingling Chen, Ziming Cai, Longtu Li, and Xiaohui Wang. High-performance relaxor ferroelectric materials for energy storage applications. *Advanced Energy Materials*, 9(17):1803048, 2019. Mentioned on the page 15.

[25] JF Scott. Ferroelectrics go bananas. *Journal of Physics: Condensed Matter*, 20(2):021001, 2007. Mentioned 2 times in the pages 15 and 33.

[26] Francesco Ricci, Sebastian E Reyes-Lillo, Stephanie A Mack, and Jeffrey B Neaton. Candidate ferroelectrics via ab initio high-throughput screening of polar materials. *npj Computational Materials*, 10(1):15, 2024. Mentioned on the page 15.

[27] Jingjin He, Junjie Li, Chuanbao Liu, Changxin Wang, Yan Zhang, Cheng Wen, Dezhen Xue, Jiangli Cao, Yanjing Su, Lijie Qiao, et al. Machine learning identified materials descriptors for ferroelectricity. *Acta Materialia*, 209:116815, 2021. Mentioned on the page 15.

[28] Leon Chua. Memristor-the missing circuit element. *IEEE Transactions on circuit theory*, 18(5):507–519, 1971. Mentioned on the page 16.

[29] Leon O Chua and Sung Mo Kang. Memristive devices and systems. *Proceedings of the IEEE*, 64(2):209–223, 1976. Mentioned on the page 16.

[30] Tingwen Huang, Yiran Chen, Zhigang Zeng, and Leon Chua. Editorial special issue for 50th birthday of memristor theory and application of neuromorphic computing based on memristor—part i. *IEEE Transactions on Circuits and Systems I: Regular Papers*, 68(11):4417–4418, 2021. Mentioned on the page 16.

[31] Feifei Yang, Jun Ma, and Fuqiang Wu. Review on memristor application in neural circuit and network. *Chaos, Solitons & Fractals*, 187:115361, 2024. Mentioned on the page 16.

[32] Victor Lopez-Richard, Igor Ricardo Filgueira e Silva, Alessandra Ames, Frederico B Sousa, Marcio Daldin Teodoro, Ingrid David Barcelos, Raphaela de Oliveira, and Alisson R Cadore. The emergence of mem-emitters. *Nano Letters*, 2024. Mentioned 2 times in the pages 16 and 45.

[33] Suhas Kumar, Xinxin Wang, John Paul Strachan, Yuchao Yang, and Wei D Lu. Dynamical memristors for higher-complexity neuromorphic computing. *Nature Reviews Materials*, 7(7):575–591, 2022. Mentioned on the page 16.

[34] Victor Lopez-Richard, Rafael Schio Wengenroth Silva, Ovidiu Lipan, and Fabian Hartmann. Tuning the conductance topology in solids. *Journal of Applied Physics*, 133(13), 2023. Mentioned 3 times in the pages 16, 25, and 28.

[35] Mario Lanza, Abu Sebastian, Wei D Lu, Manuel Le Gallo, Meng-Fan Chang, Deji Akinwande, Francesco M Puglisi, Husam N Alshareef, Ming Liu, and Juan B Roldan. Memristive technologies for data storage, computation, encryption, and radio-frequency communication. *Science*, 376(6597):eabj9979, 2022. Mentioned on the page 16.

[36] Gianluca Milano, Masakazu Aono, Luca Boarino, Umberto Celano, Tsuyoshi Hasegawa, Michael Kozicki, Sayani Majumdar, Mariela Menghini, Enrique Miranda, Carlo Ricciardi, et al. Quantum conductance in memristive devices: fundamentals, developments, and applications. *Advanced Materials*, 34(32):2201248, 2022. Mentioned on the page 16.

[37] Igor Ricardo Filgueira e Silva, Ovidiu Lipan, Fabian Hartmann, Sven Höfling, and Victor Lopez-Richard. Microscopic modeling of polarization dynamics in leaky dielectrics: Insights into ferroelectric-like behavior. *Materials Science and Engineering: B*, 316:118089, 2025. Mentioned on the page 16.

[38] Alessandra Ames, Frederico B Sousa, Gabriel AD Souza, Raphaela de Oliveira, Igor R F Silva, Gabriel L Rodrigues, Kenji Watanabe, Takashi Taniguchi, Gilmar E

Marques, Ingrid D Barcelos, et al. Optical memory in a mose _2/clinochlore device. *Applied Materials and Interface*, 2025. Mentioned on the page 17.

[39] JR Reitz, FJ Milford, and RW Christy. *Fundamentos da Teoria Eletromagnética. 3ª edição*. Editora Campus Ltda, Rio de Janeiro, 1988. Mentioned 2 times in the pages 21 and 28.

[40] Kleber Daum Machado. *Teoria do eletromagnetismo: volume 1*. UEPG, Ponta Grossa, 2007. Mentioned on the page 21.

[41] Richard P Feynman, RB Leighton, and M Sandes. *Lições de Física de Feynman*, volume 2. Bookman, Porto Alegre, 2008. Mentioned on the page 21.

[42] Roald K Wangsness and Ronald K Wangsness. *Electromagnetic fields*. John Wiley and Sons, New York, 1986. Mentioned on the page 21.

[43] Sílvio RA Salinas. *Introdução à física estatística*. Edusp, São Paulo, 1999. Mentioned 2 times in the pages 25 and 26.

[44] Eite Tiesinga, Peter J Mohr, David B Newell, and Barry N Taylor. Codata recommended values of the fundamental physical constants: 2018. *Journal of physical and chemical reference data*, 50(3), 2021. Mentioned on the page 25.

[45] Aline Bastos de Paiva, Rafael Schio Wengenroth Silva, Marcio Peron Franco de Godoy, Luis Miguel Bolaños Vargas, Marcelos Lima Peres, Demétrio AW Soares, and Victor Lopez-Richard. Temperature, detriment, or advantage for memory emergence: The case of zno. *The Journal of Chemical Physics*, 157(1), 2022. Mentioned on the page 25.

[46] David J Griffiths. *Eletrodinâmica*. Pearson/Addison-Wesley, São Paulo, 2011. Mentioned 2 times in the pages 27 and 28.

[47] Victor Lopez-Richard, Soumen Pradhan, Rafael Schio Wengenroth Silva, Ovidiu Lipan, Leonardo K Castelano, Sven Höfling, and Fabian Hartmann. Beyond equivalent circuit representations in nonlinear systems with inherent memory. *Journal of Applied Physics*, 136:165103, 2024. Mentioned 2 times in the pages 28 and 37.

[48] Victor Lopez-Richard, Soumen Pradhan, Leonardo K Castelano, Rafael Schio Wengenroth Silva, Ovidiu Lipan, Sven Höfling, and Fabian Hartmann. Accuracy bottlenecks in impedance spectroscopy due to transient effects. *Journal of Applied Physics*, 136(16), 2024. Mentioned on the page 28.

[49] Vyom Sharma, Divyansh Singh Patel, Vishal Agrawal, VK Jain, and J Ramkumar. Investigations into machining accuracy and quality in wire electrochemical

micromachining under sinusoidal and triangular voltage pulse condition. *Journal of Manufacturing Processes*, 62:348–367, 2021. Mentioned on the page 29.

[50] Yi-Yu Zhang, Shu An, Yixiong Zheng, Junyu Lai, Jung-Hun Seo, Kwang Hong Lee, and Munho Kim. Releasable algan/gan 2d electron gas heterostructure membranes for flexible wide-bandgap electronics. *Advanced Electronic Materials*, 8(2):2100652, 2022. Mentioned on the page 29.

[51] Ajeet Kumar, Geon Lee, Yeon Gyeong Chae, Atul Thakre, Han Seung Choi, Ga Hyeon Nam, and Jungho Ryu. Induced slim ferroelectric hysteresis loops and enhanced energy-storage properties of mn-doped (pb0 · 93la0. 07)(zr0 · 82ti0. 18) o3 anti-ferroelectric thick films by aerosol deposition. *Ceramics International*, 47(22):31590–31596, 2021. Mentioned on the page 29.

[52] Yoshihiro Sekine, Ryohei Akiyoshi, and Shinya Hayami. Recent advances in ferroelectric metal complexes. *Coordination Chemistry Reviews*, 469:214663, 2022. Mentioned on the page 29.

[53] Matteo Manzi, Giovanni Pica, Michele De Bastiani, Soumya Kundu, Giulia Grancini, and Makhsud I Saidaminov. Ferroelectricity in hybrid perovskites. *The Journal of Physical Chemistry Letters*, 14(14):3535–3552, 2023. Mentioned on the page 29.

[54] Nengneng Luo, Li Ma, Gengguang Luo, Chao Xu, Lixiang Rao, Zhengu Chen, Zhenyong Cen, Qin Feng, Xiyong Chen, Fujita Toyohisa, et al. Well-defined double hysteresis loop in nanbo3 antiferroelectrics. *Nature communications*, 14(1):1776, 2023. Mentioned on the page 31.

[55] Qi-Kun Feng, Shao-Long Zhong, Jia-Yao Pei, Yu Zhao, Dong-Li Zhang, Di-Fan Liu, Yong-Xin Zhang, and Zhi-Min Dang. Recent progress and future prospects on all-organic polymer dielectrics for energy storage capacitors. *Chemical Reviews*, 122(3):3820–3878, 2021. Mentioned on the page 31.

[56] Chun-Yuan Wang, Chin-I Wang, Sheng-Han Yi, Teng-Jan Chang, Chun-Yi Chou, Yu-Tung Yin, Makoto Shiojiri, and Miin-Jang Chen. Paraelectric/antiferroelectric/-ferroelectric phase transformation in as-deposited zro2 thin films by the tin capping engineering. *Materials & Design*, 195:109020, 2020. Mentioned on the page 31.

[57] Lucian Pintilie, Ksenia Boldyreva, Marin Alexe, and Dietrich Hesse. Coexistence of ferroelectricity and antiferroelectricity in epitaxial pbzro3 films with different orientations. *Journal of Applied Physics*, 103(2), 2008. Mentioned on the page 31.

[58] X-H Wei, Ralph Skomski, Z-G Sun, and David J Sellmyer. Proteresis in co: Coo core-shell nanoclusters. *Journal of Applied Physics*, 103(7), 2008. Mentioned on the page 31.

[59] Azeemuddin Syed, Mohamad Tafazoli, Nima Davoudzadeh, and MR Sayeh. An all-optical proteretic switch using semiconductor ring lasers. *Optics Communications*, 475:126252, 2020. Mentioned on the page 31.

[60] Salma Khan, Syed Azeemuddin, and Mohammed Arifuddin Sohel. Prohys puf: A proteresis-hysteresis switch based physical unclonable function. *Integration*, 89:207–216, 2023. Mentioned on the page 31.

[61] Pascal Girard and Jean-Pierre Boissel. Clockwise hysteresis or proteresis. *Journal of pharmacokinetics and biopharmaceutics*, 17:401–402, 1989. Mentioned on the page 31.

[62] Xiaoyong Wei, Yujun Feng, Lianmao Hang, Song Xia, Li Jin, and Xi Yao. Abnormal c–v curve and clockwise hysteresis loop in ferroelectric barium stannate titanate ceramics. *Materials Science and Engineering: B*, 120(1-3):64–67, 2005. Mentioned on the page 31.

[63] D-G Jin, S-G Kim, H Jeon, E-J Park, S-H Kim, J-Y Kim, and H-Y Yu. Improvement of polarization switching in ferroelectric transistor by interface trap reduction for brain-inspired artificial synapses. *Materials Today Nano*, 22:100320, 2023. Mentioned on the page 31.

[64] John T. S. Irvine, Derek C. Sinclair, and Anthony R. West. Electroceramics: Characterization by impedance spectroscopy. *Advanced Materials*, 2(3):132–138, 1990. Mentioned on the page 34.

[65] Evgenij Barsoukov and J. Ross Macdonald, editors. *Impedance Spectroscopy: Theory, Experiment, and Applications*. John Wiley & Sons, Inc., Hoboken, NJ, USA, third edition edition, 2018. Second edition: 2005, John Wiley & Sons, Inc. Mentioned 2 times in the pages 34 and 40.

[66] W. H. Hunter Woodward. *Broadband Dielectric Spectroscopy—A Practical Guide*, volume 1375. ACS Symposium Series, Midland, Michigan, 2021. Mentioned 2 times in the pages 34 and 41.

[67] Noel A. Clark, Xi Chen, Joseph E. MacLennan, and Matthew A. Glaser. Dielectric spectroscopy of ferroelectric nematic liquid crystals: Measuring the capacitance of insulating interfacial layers. *Phys. Rev. Res.*, 6:013195, Feb 2024. Mentioned on the page 34.

[68] Mary L Boas. *Mathematical methods in the physical sciences*. John Wiley & Sons, Danvers, 2006. Mentioned on the page 35.

[69] Afshin Izadian. *Fundamentals of Modern Electric Circuit Analysis and Filter Synthesis*. Springer, Cham,Switzerland, 2019. Mentioned on the page 37.

[70] Charles K Alexander, Matthew NO Sadiku, and Matthew Sadiku. *Fundamentals of electric circuits*. McGraw-Hill Higher Education, New York, 2017. Mentioned on the page 37.

[71] Divya Priyadarshani, Debittree Choudhury, Miji E Joy, Anil Kottantharayil, and Manoj Neergat. Electrochemical investigation of si of various dopant concentrations at negative overpotentials in aqueous electrolyte. *The Journal of Physical Chemistry C*, 125(50):27736–27746, 2021. Mentioned 2 times in the pages 38 and 49.

[72] Agustín Bou, Adam Pockett, Dimitrios Raptis, Trystan Watson, Matthew J Carnie, and Juan Bisquert. Beyond impedance spectroscopy of perovskite solar cells: insights from the spectral correlation of the electrooptical frequency techniques. *The Journal of Physical Chemistry Letters*, 11(20):8654–8659, 2020. Mentioned 2 times in the pages 38 and 49.

[73] Sumayya M Abdulrahim, Zubair Ahmad, Muhammad Qasim Mehmood, Sanghyun Paek, J Bhadra, Noora J Al-Thani, Mohammad Khaja Nazeeruddin, Abdelhak Belaidi, and Mahmood Amani. Effect of illumination and applied potential on the electrochemical impedance spectra in triple cation (fa/ma/cs) 3d and 2d/3d perovskite solar cells. *Journal of Electroanalytical Chemistry*, 902:115800, 2021. Mentioned 2 times in the pages 38 and 49.

[74] Arun Thapa and Hongwei Gao. Low-frequency inductive loop and its origin in the impedance spectrum of a graphite anode. *Journal of The Electrochemical Society*, 169(11):110535, 2022. Mentioned 2 times in the pages 38 and 49.

[75] Salil M Joshi, Ning Xia, Yolande Berta, Yong Ding, Rosario A Gerhardt, Kenneth C Littrell, Eric Woods, and Mengkun Tian. Detection of plasmonic behavior in colloidal indium tin oxide films by impedance spectroscopy. *MRS Communications*, 10(2):278–285, 2020. Mentioned 3 times in the pages 38, 40, and 49.

[76] G Ramesh, MS Ramachandra Rao, V Sivasubramanian, and V Subramanian. Electrocaloric effect in (1- x) pin-xpt relaxor ferroelectrics. *Journal of Alloys and Compounds*, 663:444–448, 2016. Mentioned 2 times in the pages 44 and 49.

[77] Yong Zhou, Ke Xiong, Shuyu Wu, Luqi Tu, Xudong Wang, Yan Chen, Shuaiqin Wu, Jinhua Zeng, Yuqing Zheng, Shiqun Gu, et al. Anomalous polarization-switching phenomena and noteworthy pyroelectricity in ferroelectric hf0. 5zr0. 5o2 polycrystalline films. *Materials Today Physics*, 43:101414, 2024. Mentioned 2 times in the pages 44 and 49.

[78] Teng Tan, Xiantao Jiang, Cong Wang, Baicheng Yao, and Han Zhang. 2d material optoelectronics for information functional device applications: status and challenges. *Advanced Science*, 7(11):2000058, 2020. Mentioned on the page 45.

[79] Massimiliano Di Ventra, Yuriy V. Pershin, and Leon O. Chua. Circuit elements with memory: Memristors, memcapacitors, and meminductors. *Proceedings of the IEEE*, 97(10):1717–1724, 2009. Mentioned on the page 45.

[80] Simone Bertolazzi, Daria Krasnozhon, and Andras Kis. Nonvolatile memory cells based on mos2/graphene heterostructures. *ACS nano*, 7(4):3246–3252, 2013. Mentioned on the page 46.

[81] Sajedeh Manzeli, Dmitry Ovchinnikov, Diego Pasquier, Oleg V Yazyev, and Andras Kis. 2d transition metal dichalcogenides. *Nature Reviews Materials*, 2(8):1–15, 2017. Mentioned on the page 46.

Appendix

APPENDIX A – Table of Parameters

Figure	$\tau^{(lk)}/\tau^{(p)}$	$\lambda^{(lk)}/\lambda^{(p)}$	η	α	β	C	G_0
4(b)	——/1.0	——/2.0	0.005	0.01/1.0/100	0.0/0.1	0.05	——
4(c)	——/1.0	——/2.0	0.005	0.01/1.0/100	0.1	0.05	——
4(d)	——/1.0	——/2.0	0.005	0.01/1.0/100	0.1	0.05	——
4(e)	——/1.0	——/6.0 $\times 10^{-10}$	0.48/0.50/0.52	1.0	0.2	0.05	——
4(f)	——/1.0	——/6.0 $\times 10^{-10}$	0.48/0.50/0.52	1.0	0.2	0.05	——
4(g)	——/1.0	——/6.0 $\times 10^{-10}$	0.48/0.50/0.52	1.0	0.2	0.05	——
4(h)	1.0/0.1	10.0/50.0	0.01	1.0	——	0.5	1.0
4(i)	1.0/0.5	10.0/50.0	0.01	1.0	——	0.5	1.0
4(j)	1.0/1.0	10.0/50.0	0.01	1.0	——	0.5	1.0
4(k)	1.0/0.1	10.0/50.0	0.01	1.0	——	0.5	1.0
4(l)	1.0/0.5	10.0/50.0	0.01	1.0	——	0.5	1.0
4(m)	1.0/1.0	10.0/50.0	0.01	1.0	——	0.5	1.0
5(b)	——/1.0	——/2.0	0.005	1.0	0.1	0.05	——
5(c)	——/1.0	——/6.0 $\times 10^{-10}$	0.48/0.50/0.52	1.0	0.2	0.05	——
5(d)	——/1.0	——/2.0	0.005	1.0	0.1	0.05	——
5(e)	——/1.0	——/6.0 $\times 10^{-10}$	0.48/0.50/0.52	1.0	0.2	0.05	——
5(f)	1.0/0.1	10.0/50.0	0.01	1.0	——	0.5	1.0
5(g)	1.0/0.5	10.0/50.0	0.01	1.0	——	0.5	1.0
5(h)	1.0/1.0	10.0/50.0	0.01	1.0	——	0.5	1.0
5(i)	1.0/0.1	10.0/50.0	0.01	1.0	——	0.5	1.0
5(j)	1.0/0.5	10.0/50.0	0.01	1.0	——	0.5	1.0
5(k)	1.0/1.0	10.0/50.0	0.01	1.0	——	0.5	1.0
7(a)	1.0/0.1	1.0/2.0	0.01	10.0	——	0.01	1.0
7(b)	1.0/0.1	1.0/2.0	0.01	10.0	——	0.01	1.0
8(a)	1.0/0.1	1.0/2.0	0.01	10.0	——	0.01	1.0
8(b)	1.0/0.1	1.0/2.0	0.01	10.0	——	0.01	1.0
8(c)	1.0/0.1	1.0/2.0	0.01	10.0	——	0.01	1.0
8(d)	1.0/0.1	1.0/2.0	0.01	10.0	——	0.01	1.0
9(a)	1.0/0.1	———	10.0	——	——	——	
9(b)	1.0/0.1	———	10.0	——	——	——	

Table 1 – The table above provides a detailed list of all the parameters used in the construction of the figures presented throughout this work.